On the Mechanics of Natural Compliance in Frictional Contacts and its Effect on Grasp Stiffness and Stability

Amir Shapiro*
Dept. of ME
Ben Gurion University
ashapiro@bgu.ac.il

Elon Rimon
Dept. of ME
Technion
rimon@technion.ac.il

Alon Ohev–Zion
Dept. of ME
Ben Gurion University
alonohev@bgu.ac.il

Abstract *This paper considers the effect of natural material compliance on the stiffness and stability of frictional multi-contact grasps and fixtures. The contact preload profile is a key parameter in the nonlinear compliance laws governing such contacts. The paper introduces the Hertz-Walton contact compliance model which is valid for linear contact loading profiles. The model is specified in a lumped parameter form suitable for on-line grasping applications, and is entirely determined by the contact friction and by the material and geometric properties of the contacting bodies. The model predicts an asymmetric stiffening of the tangential reaction force as the normal load at the contact increases. As a result, the composite stiffness matrix of multi-contact grasps governed by natural compliance effects is asymmetric, indicating that these contact arrangements are not governed by any potential energy function. The implication of asymmetric grasp stiffness matrices on grasp stability is investigated. Based on the compliant grasp dynamics, the paper derives rules indicating which contact point locations and what preload profiles guarantee grasp and fixture stability. The paper also describes preliminary experiments supporting the contact model predictions.*

1 Introduction

This paper considers the effect of natural material compliance in frictional multi-contact arrangements. Natural friction-compliance effects play a key role in several grasping applications. For instance, biomimetic multi-finger hands are currently being developed for handling delicate objects such as fruits and vegetables [30, 40]. Such hands are typically designed with soft fingertips [14, 29], and the determination of grasp stability during object handling is a

*Corresponding author: Dept. of ME, Ben Gurion University, Beer-Sheva, Israel.

key component of these systems [25, 36, 46]. Natural contact compliance also plays an important role in quasistatic locomotion synthesis. When a multi-limbed or snake-like robot moves quasistatically by embracing against the environment, natural force-displacement laws at the contacts influence the mechanism's overall stability [32, 34]. A similar observation holds for whole arm manipulation, where a robot arm is allowed to establish mid-link contacts with the manipulated object [10, 28]. Due to the passive nature of the mid-link contacts, the stability of whole-arm grasps requires a consideration of the natural friction-compliance laws at the contacts [44]. Industrial fixturing may also benefit from friction-compliance stability models. Current fixturing practice immobilizes a given workpiece using redundant form closure grasps (e.g. [4, 16]). This costly and time consuming practice relies on frictionless rigid-body constraints imposed by the fixturing elements [3, 15]. Sound understanding how natural compliance affects the stiffness and stability of grasps that rely on friction effects may allow more economic fixtures that use a smaller number of contacts.

The natural stiffness and stability of multi-contact arrangements is determined by nonlinear compliance laws. When these laws model frictional compliant contacts, they require explicit consideration of the contact loading profiles. The Hertz-Walton model provides an analytic compliance law under the assumption of *linear* contact loading profiles. Based on this model, the current paper analyzes the stiffness and stability of multi-contact grasps and fixtures and derives rules indicating which contact force magnitudes and what preload profiles guarantee stable grasps. The relevant literature can be divided into compliance models proposed in the solid mechanics literature, and compliant grasp analysis and synthesis tools developed in the robotics literature.

In the solid mechanics literature, the modeling of the *normal* force due to natural compliance effects is based on the classical model of Hertz [12]. The main focused effort on modeling the natural *tangential* compliance at a non-slipping frictional contact is by Mindlin and Deresiewicz [23, 24]. They investigated the case where a contact is initially loaded along the normal direction in accordance with the Hertz compliance model. Then they analyzed the tangential traction field generated by applying pure tangential loads while the normal load remains constant. Their investigation revealed highly nonlinear and complex phenomena such as micro-slip and hysteresis. Moreover, researchers in this field have come to realize that the tangential force-displacement law depends on the contact's loading profile [19][p. 221]. Motivated by granular material packing applications, Walton [41] derived an analytic tangential compliance model which is much more relevant for grasping and fixturing applications. This model was later refined by Elata and Berryman [6]. Walton assumes that a contact is loaded along some *linear loading profile.* Under this assumption (and using a different analysis approach than Mindlin's), he derived an analytic model for the tangential compliance force at a frictional contact. The normal force component in Walton's model satisfies the Hertz law, and the combined Hertz-Walton model will be the basis for the

investigation conducted in this paper. The solid mechanics literature also offers numerical compliance models based on finite-element analysis (e.g. [7, 45]). However, analytic lumped-parameter models provide the insight and computational simplicity required for automated grasp and fixture planning [18, 20].

In the robotics literature, the stability of compliant multi-contact grasps is determined by their *stiffness matrix*, giving the linearized relation between small movements of the grasped object and the net reaction wrench (force and torque) generated by the contacts. Early papers model natural compliance effects by postulating linear springs that act in tandem with a rigid-body Coulomb friction law [1, 8]. A positive definite Hessian matrix of the springs' elastic potential energy ensures stability of such grasps [27, 43]. However, the linear spring approach is not supported by the solid mechanics literature. In particular, without knowledge of an underlying nonlinear contact model there is no way to predict the linear spring coefficients. Moreover, it is intuitively clear (and rigorously justified below) that the contacts experience tangential stiffening as the bodies are pressed harder together. Subsequent papers focused on the inclusion of the Hertz normal compliance model into the analysis and synthesis of *frictionless* grasps and fixtures [17, 21, 22, 46]. The first systematic efforts at incorporating *frictional* compliance effects were made by Sinha and Abel [35, 20, 42]. However, they proposed a discretized friction-compliance contact model akin to the finite-element approach.

This paper considers analytic compliance models that allow closed form analysis and synthesis of stable grasps. Such analytic models have been proposed by Hirai et al. [18] and Xiong et al. [44]. Hirai et al. model soft fingertips as a continuoum of linear spring aligned with the finger's initial contact normal [18]. Based on the fingertip shape, they derived a power low which describes the elastic potential energy stored in the compressed fingertip. The potential energy associated with several fingertips was subsequently used to synthesize stable manipulation plans. Xiong et al. combined Sinha and Abel's contact model with the Hertz normal compliance model [44]. They obtained a nonlinear compliance model which predicts the normal and tangential contact reaction forces, and applied this model to the prediction of stability and force closure in whole-arm grasps. Our paper complements the existing papers in three fundamental ways. First, the existing compliance models require that the contacts be preloaded only along the contact normals. The Hertz-Walton model discussed in this paper allows any linear loading of the contacts. Second, they judge the stability of a candidate grasp by constructing a potential energy function and computing its Hessian matrix. While a potential-function approach may be justified under normal loading profiles, this paper establishes that under general linear loading profiles the resulting grasp is not governed by any potential energy function. Third, the current paper emphasizes the role of the contact loading profile in ensuring grasp stability, a topic which has not yet been discussed in the robotics literature.

The paper is structured as follows. Section 2 describes the Hertz-Walton compliance model associated with linear contact loading profiles. Section 3 focuses on the stiffness matrices of the individual contacts, which are shown to be *asymmetric* under the Hertz-Walton model. Section 3 derives the grasp stiffness matrix associated with the Hertz-Walton model. The grasp stiffness matrix is *asymmetric,* thus indicating that the dynamics of os such grasps is *not* governed by any potential energy function. To establish the stability of these grasps, Section 3 characterizes which linear loadings profiles guarantee stable response at the individual contacts. Based on this characterization, Section 4 analyzes the composite grasp dynamics and derives a criterion for achieving compliantly stable grasps. Section 5 discusses guidelines for selecting the contact point locations and the loading profiles which give compliantly stable grasps. Section 6 describes experiments which verify the Hertz-Walton model using compliant fingertips. The concluding section discusses `extension to 3D` and on-going experimental validation of the model predictions.

2 Friction-Compliance Models

This section describes the Hertz and Walton compliance models in a configuration-space setting. Assume that a 3D object $\mathcal{B}$ is held stationary by 3D bodies $\mathcal{A}_1, \ldots, \mathcal{A}_k$ representing fingertips or fixels. The usual assumption made in the solid mechanics literature is that the contacting bodies are *quasi-rigid*, meaning that their deformations due to natural compliance effects are localized to the vicinity of the contacts [19]. This assumption is generally valid for all bodies which are not made of exceptionally soft material and do not contain slender substructures [46]. The quasi-rigidity assumption allows us to describe the overall motion of $\mathcal{B}$ relative to the stationary bodies $\mathcal{A}_1, ..., \mathcal{A}_k$ using rigid body kinematics. Since the grasping bodies are essentially stationary, one can focus on $\mathcal{B}$'s configuration space, or *c-space.*

This paper considers the nonlinear compliance models in the context of planar configuration spaces. We assume that the bodies lie on a frictionless supporting plane, such that the bodies interact via frictional forces parallel to the supporting plane. The planar configuration of $\mathcal{B}$ is parametrized by $q = (d, \theta) \in \mathbb{R}^2 \times \mathbb{R}$, where d and θ are $\mathcal{B}$'s position and orientation relative to a fixed reference frame. The velocities of $\mathcal{B}$ are denoted $\dot{q} = (v, \omega) \in \mathbb{R}^2 \times \mathbb{R}$, where v and ω are $\mathcal{B}$'s linear and angular velocities. The wrenches acting on $\mathcal{B}$ are denoted $\boldsymbol{w} = (f, \tau) \in \mathbb{R}^2 \times \mathbb{R}$, where f and τ are the force and torque acting on $\mathcal{B}$. Note that $\boldsymbol{w}$ acts as a covector on $\dot{q}$, with $\boldsymbol{w} \cdot \dot{q}$ corresponding to the physical power transmitted to $\mathcal{B}$ during its instantaneous motion along $\dot{q}$.

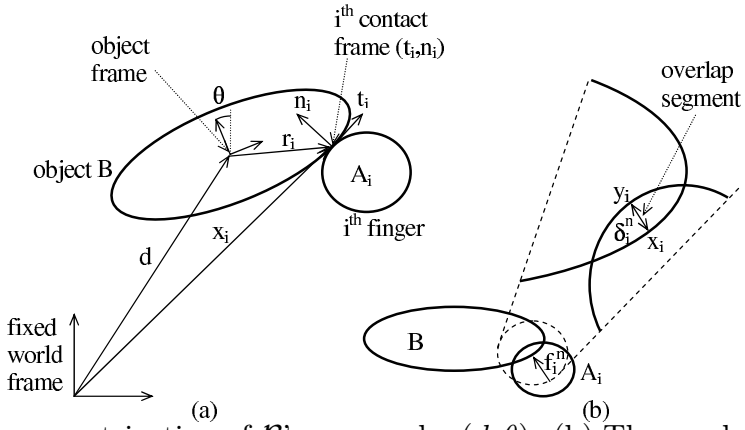

Figure 1: (a) The parametrization of $\mathcal{B}$'s c-space by (d, θ). (b) The overlap segment between $\mathcal{B}$ and $\mathcal{A}_i$ and the net normal force acting along this segment.

2.1 Normal Compliance Models

Let us first describe a generic normal compliance modeling approach which ignores the details of compliant surface deformation and models the resultant contact force as a function of $\mathcal{B}$'s configuration [21]. Consider a single contact between $\mathcal{B}$ and $\mathcal{A}_i$. In the absence of deformation, the two bodies contact at a single point. When pushed together, the two contacting surfaces deform. One can conceptually think of the two rigid bodies as interpenetrating, or overlapping with their undeformed shapes, as illustrated in Figure 1(b). When $\mathcal{B}$ is located at a configuration q, the *overlap*[1] between $\mathcal{B}$ and $\mathcal{A}_i$, denoted $\delta_i^n(q)$, is the minimum amount of translation of $\mathcal{B}$ that would separate it from $\mathcal{A}_i$. The *overlap segment* is the unique segment whose endpoints lie on the surfaces of $\mathcal{B}$ and $\mathcal{A}_i$, such that the length of the segment is δ_i^n and its orientation gives the direction of separating translation. For sufficiently small δ_i^n, the overlap segment is collinear with the normals to the surfaces of $\mathcal{B}$ and $\mathcal{A}_i$. In this lumped parameter form of modeling, the net normal force induced by the local deformation is assumed to act at $\mathcal{B}$'s endpoint of the overlap segment, x_i, along the inward pointing direction of the overlap segment, n_i (Figure 1). The normal component of the contact force, f_i^n, is assumed to depend on δ_i^n in terms of a function $g_i(\delta_i^n)$. This function is required to be differentiable, zero when δ_i^n is zero, and monotonically increasing when δ_i^n is positive. The normal component of the contact force, f_i^n, obeys a generic law of the form:

$$f_i^n = g_i(\delta_i^n) + \delta_i^n \cdot \varphi_i^n(\dot{\delta}_i^n)$$
$$\text{such that } g_i'(\delta_i^n) > 0 \text{ when } \delta_i^n > 0.$$

[1]The notion of overlap used here is consistent with the concept of "relative approach" in contact mechanics [19].

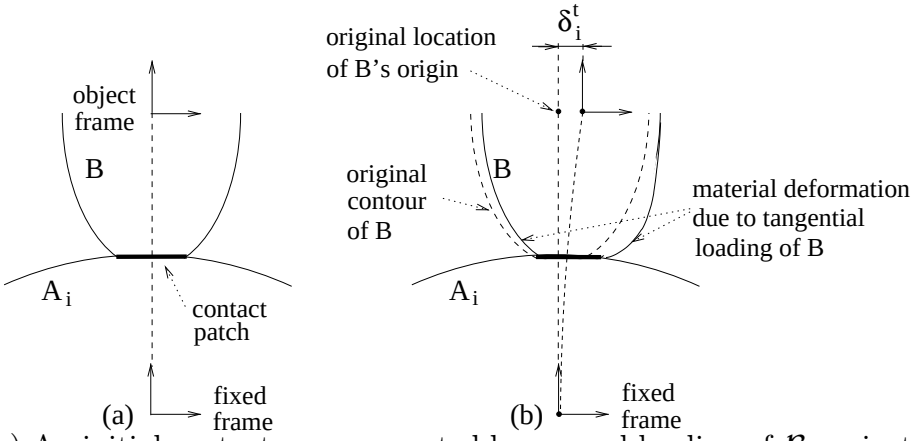

Figure 2: (a) An initial contact area generated by normal loading of $\mathcal{B}$ against $\mathcal{A}_i$. (b) Tangential loading of $\mathcal{B}$ causes tangential displacement of $\mathcal{B}$ without any macro-slip.

It is important to note that a wide variety of contact models can be represented under this generic law. The simplest contact model assumes that g_i is a linear function of the overlap, $g_i(\delta_i^n) = \kappa_i \delta_i^n$, where the coefficient κ_i represents the combined stiffness of $\mathcal{B}$ and $\mathcal{A}_i$ at the contact [17]. The function φ_i^n represents damping due to viscoelastic effects. It is required to be differentiable, zero when $\dot{\delta}_i^n$ is zero, and monotonically increasing in $\dot{\delta}_i^n$. Since the damping force acts along $\mathcal{B}$'s inward contact normal when $\varphi_i^n > 0$, it resists $\mathcal{B}$'s penetration into $\mathcal{A}_i$ when $\dot{\delta}_i^n > 0$ and resists $\mathcal{B}$'s motion away from $\mathcal{A}_i$ when $\dot{\delta}_i^n < 0$.

The Hertz normal compliance model [12]. The nonlinear Hertz model which has been verified experimentally [19], establishes that for two quasi-rigid bodies $\mathcal{A}_i$ and $\mathcal{B}$ with spherical tips of radii $r_{\mathcal{A}_i}$ and $r_{\mathcal{B}_i}$:

$$g_i(\delta_i^n) = \frac{8G\sqrt{r_i}}{3(1-\nu)}(\delta_i^n)^{3/2}, \tag{1}$$

where $r_i = r_{\mathcal{A}_i} r_{\mathcal{B}_i}/(r_{\mathcal{A}_i} + r_{\mathcal{B}_i})$, G is the material's modulus of rigidity expressed in $\mathsf{N/m^2}$, and ν is the material's Poisson ratio. The Poisson ratio is a unitless parameter satisfying $0 \leq \nu \leq 0.5$ for all practical materials [19]. The Hertzian law is sometimes expressed in terms of the material's modulus of elasticity, E, rather than G, where $E = 2G(1+\nu)$.

2.2 Tangential Compliance Models

The process underlying tangential compliance at a frictional contact is as follows. When two quasi-rigid bodies are preloaded along the normal direction, they locally deform and estab-

lish a contact area centered at the original contact point (Figure 2(a)). The deformed bodies generate a normal force-field which is continuously distributed along the contact area (its integral over the contact area gives the net normal force f_i^n). When the two bodies are next loaded along a tangential direction, they locally deform in a way that generates a tangential force-field which is again continuously distributed along the contact area (Figure 2(b)). The usual assumption made in the solid mechanics literature is that *the normal and tangential force fields interact at the individual points of the contact area according to Coulomb's law* [24]. Under this assumption, elasticity theory as well as experiments indicate that the tangential force-field consists of two regimes. At points in an outer ring of the contact area the tangential forces exceed the friction cone constraint, causing micro-slip at these points. At points along the complementary inner disc of the contact area the tangential forces lie within the friction cone, and at these points no micro-slip takes place. As the magnitude of the tangential loading increases the area of the stationary inner disc shrinks. Finally, when the net tangential force reaches μf_i^n (μ being the coefficient of friction), the inner disc shrinks to a point and the two bodies experience macro-slip at the contact.

Based on this insight, we formulate a generic tangential compliance law, assuming that the contacting bodies deform but do not slip. This law covers most of the tangential compliance models proposed in the literature [6, 24, 41], and is therefore quite general. Recall that x_i is $\mathcal{B}$'s endpoint of the overlap segment. Let r_i denote the same point expressed in $\mathcal{B}$'s body frame (Figure 1(a)). Then x_i is related to r_i by the rigid-body transformation: $x_i = X(r_i, q) = R(\theta)r_i + d$, where $R(\theta)$ is $\mathcal{B}$'s orientation matrix. Let $X_{r_i}(q)$ denote the transformation $X(r_i, q)$ such that r_i is held fixed. When $\mathcal{B}$ moves along a c-space trajectory $q(t)$, the velocity of X_{r_i} is given by $\frac{d}{dt}X_{r_i}(q(t)) = G_i\dot{q}(t)$, where $G_i = DX_{r_i}$ is the 2×3 Jacobian matrix of X_{r_i}. Let $\delta_i^t(q(t))$ denote the tangential displacement of $\mathcal{B}$ relative to the i^{th} contact due to $\mathcal{B}$'s motion along $q(t)$ (Figure 2(b)). Let t_i denote the unit tangent to $\mathcal{B}$'s boundary at x_i. The derivative of δ_i^t along $q(t)$ is given by the projection of $\dot{X}_{r_i}$ along t_i:

$$\frac{d}{dt}\delta_i^t(q(t)) = t_i \cdot \dot{X}_{r_i} = t_i \cdot G_i\dot{q}(t). \tag{2}$$

In contrast with $\delta_i^n(q)$, the tangential displacement is *not* a direct function of q, but requires integration of (2) over the entire loading trajectory [19][p. 221]. The tangential component of the contact force, f_i^t, obeys a generic law of the form:

$$f_i^t = -h_i(\delta_i^t, \delta_i^n) - \delta_i^n \cdot \varphi_i^t(\dot{\delta}_i^t)$$
$$\text{as long as } f_i^n > 0 \text{ and } |f_i^t| < \mu f_i^n,$$

where μ is the coefficient of friction. Note that the function representing the elastic component of the tangential force, $h_i(\delta_i^t, \delta_i^n)$, depends both on the tangential and normal displacements. This function is required to be differentiable, zero when δ_i^n is zero, and for any fixed

positive δ_i^n monotonically increasing in δ_i^t. The negative sign preceding h_i implies that the tangential force *opposes* the direction of tangential displacement. The function φ_i^t represents damping due to micro-slip. It is required to be differentiable, zero when $\dot{\delta}_i^t$ is zero, and monotonically increasing in $\dot{\delta}_i^t$. The negative sign preceding φ_i^t indicates that its force resists the instantaneous change in δ_i^t.

Walton's tangential compliance model [41]. Walton assumes that a contact is loaded along a linear loading profile satisfying $\delta_i^t = c_i \delta_i^n$, such that c_i is constant throughout the loading process. Let two quasi-rigid bodies $\mathcal{A}_i$ and $\mathcal{B}$ have spherical tips of radii $r_{\mathcal{A}_i}$ and $r_{\mathcal{B}_i}$. When the two bodies are preloaded with a linear loading profile, the function h_i is given by

$$h_i(\delta_i^t, \delta_i^n) = \frac{16G\sqrt{r_i}}{3(2-\nu)} \sqrt{\delta_i^n}\, \delta_i^t \qquad \text{as long as } \delta_i^n > 0 \text{ and } |c_i| < \mu \frac{(2-\nu)}{2(1-\nu)}, \tag{3}$$

where G and ν are specified above, $r_i = r_{\mathcal{A}_i} r_{\mathcal{B}_i} / (r_{\mathcal{A}_i} + r_{\mathcal{B}_i})$, and μ is the friction coefficient at the contact. The condition $|c_i| < \mu \frac{(2-\nu)}{2(1-\nu)}$ results from substituting formulas (1) and (3) for f_i^n and f_i^t in the friction cone constraint $|f_i^t| < \mu f_i^n$. Walton's formula is extremely relevant for grasping and fixturing applications, since one can readily implement a linear preloading of the contacts. Note that (3) indicates a nonlinear tangential stiffening at the contact for larger normal penetrations. Walton's formula agrees up to constants with the tangential compliance model obtained by Mindlin and Deresiewicz [23, 24]. However, the Mindlin and Deresiewicz model assumes pure normal loading followed by pure tangential loading, while the Walton model allows any linear loading profile.

3 The Individual Contact Stiffness Matrices

When a quasi-rigid object $\mathcal{B}$ is held in a compliant equilibrium grasp, the grasp's stability is determined by the net wrench induced on $\mathcal{B}$ by the contacts in response to small displacements of $\mathcal{B}$. This section characterizes the wrench induced on $\mathcal{B}$ by the individual contacts under the Hertz-Walton compliance model. Let q_0 denote the object's equilibrium grasp configuration, which is assumed to be preloaded in accordance with the Hertz-Walton model. Denote by f_i the i^{th} contact force acting on $\mathcal{B}$ at x_i, described in a fixed reference frame. Denote by t_i and n_i the unit tangent and inward unit normal to $\mathcal{B}$ at x_i, and by $R_i(q_0) = [t_i\, n_i]$ the 2×2 orientation matrix of the i^{th} contact frame at q_0. The force f_i is given by

$$f_i = R_i(q_0) \begin{pmatrix} f_i^t \\ f_i^n \end{pmatrix},$$

where (f_i^t, f_i^n) are specified in terms of (δ_i^t, δ_i^n) by the Hertz-Walton model. The i^{th} *contact stiffness matrix*, $K_i(q_0)$, is the 2×2 matrix representing the linearized force-displacement relationship at the i^{th} contact:

$$\begin{pmatrix} \Delta f_i^t \\ \Delta f_i^n \end{pmatrix} = K_i(q_0) \begin{pmatrix} \Delta \delta_i^t \\ \Delta \delta_i^n \end{pmatrix}, \tag{4}$$

where $K_i(q_0)$ is specified below. The matrix $K_i(q_0)$ induces a wrench-displacement relationship in $\mathcal{B}$'s c-space as follows. Let $\Delta q = q - q_0$ denote a small c-space displacement of $\mathcal{B}$ about q_0. Let $\Delta \boldsymbol{w}_i$ be the wrench generated by the i^{th} contact on $\mathcal{B}$ due to the displacement Δq. Using the notation $\boldsymbol{\delta}_i(q) = (\delta_i^t(q), \delta_i^n(q))$, the pair $(\Delta f_i^t, \Delta f_i^n)$ is related to Δq by

$$\begin{pmatrix} \Delta f_i^t \\ \Delta f_i^n \end{pmatrix} = K_i(q_0) D\boldsymbol{\delta}_i(q_0) \Delta q, \tag{5}$$

where $D\boldsymbol{\delta}_i$ is the 2×3 Jacobian of $\boldsymbol{\delta}_i(q)$. The wrench induced by $(\Delta f_i^t, \Delta f_i^n)$ on $\mathcal{B}$ is given by $\Delta \boldsymbol{w}_i = G_i^T R_i \begin{pmatrix} \Delta f_i^t \\ \Delta f_i^n \end{pmatrix}$, where $G_i = DX_{r_i}$ is the 2×3 Jacobian of X_{r_i}. Multiplying both sides of (5) by $G_i^T R_i$ gives the c-space relation:

$$\Delta \boldsymbol{w}_i = \left[G_i^T(q_0) R_i(q_0) K_i(q_0) D\boldsymbol{\delta}_i(q_0) \right] \Delta q = \tilde{K}_i(q_0) \Delta q.$$

The 3×3 matrix $\tilde{K}_i(q_0)$ is the linearized wrench-displacement relationship induced on $\mathcal{B}$ by the i^{th} contact.

We now derive formulas for $K_i(q_0)$ and $\tilde{K}_i(q_0)$ based on the Hertz-Walton model. Walton's law assumes a linear loading profile. It is therefore valid only for small changes $(\Delta \delta_i^t, \Delta \delta_i^n)$ aligned with the nominal loading profile. On the other hand, $K_i(q_0)$ gives the contact reaction force in response to arbitrary small displacements $(\Delta \delta_i^t, \Delta \delta_i^n)$. To obtain a formula for $K_i(q_0)$, we introduce the practical assumption that *closely matching loading profiles generate closely matching tangential traction fields.* Under this assumption the tangential traction field resulting from a linear loading followed by arbitrary small displacements can be obtained from the Hertz-Walton model. The formulas for $K_i(q_0)$ and $\tilde{K}_i(q_0)$ are as follows.

Lemma 3.1. *Let two quasi-rigid bodies $\mathcal{A}_i$ and $\mathcal{B}$ with spherical tips of radii $r_{\mathcal{A}_i}$ and $r_{\mathcal{B}_i}$ be preloaded along a linear path $\delta_i^t(q) = c_i \delta_i^n(q)$ such that $|c_i| < \mu \frac{(2-\nu)}{2(1-\nu)}$. The i^{th} contact stiffness matrix under the Hertz-Walton law is the 2×2 matrix:*

$$K_i(q_0) = 4G\sqrt{r_i}\sqrt{\delta_i^n(q_0)} \begin{bmatrix} -\frac{4}{3(2-\nu)} & -\frac{2c_i}{3(2-\nu)} \\ 0 & \frac{1}{1-\nu} \end{bmatrix}, \tag{6}$$

where $\delta_i^n(q_0)$ *is the normal penetration,* $r_i = r_{\mathcal{A}_i} r_{\mathcal{B}_i}/(r_{\mathcal{A}_i} + r_{\mathcal{B}_i})$*, and* G *and* ν *are the material's shear modulus and Poisson ratio. The c-space stiffness matrix induced by* $K_i(q_0)$ *is the* 3×3 *matrix:*

$$\tilde{K}_i(q_0) = -4G\sqrt{r_i}\sqrt{\delta_i^n(q_0)}G_i^T(q_0)R_i(q_0)\begin{bmatrix} \frac{4}{3(2-\nu)} & -\frac{2c_i}{3(2-\nu)} \\ 0 & \frac{1}{1-\nu} \end{bmatrix} R_i^T(q_0)G_i(q_0), \tag{7}$$

where $R_i(q_0) = [t_i\, n_i]$ *and* $G_i = DX_{r_i}$.

Note that $K_i(q_0)$ and consequently $\tilde{K}_i(q_0)$ are *asymmetric* matrices. The implication of this asymmetry on the stiffness and stability of multi-contact grasps is investigated in the next section.

Proof: The formula for $K_i(q_0)$ is obtained by taking the derivative of (f_i^t, f_i^n) given in (1) and (3) with respect to (δ_i^t, δ_i^n), then substituting the loading path relation $\delta_i^t(q_0) = c_i\delta_i^n(q_0)$. Next consider the 3×3 matrix $\tilde{K}_i(q_0) = G_i^T(q_0)R_i(q_0)K_i(q_0)D\boldsymbol{\delta}_i(q_0)$. Since $\boldsymbol{\delta}_i = (\delta_i^t, \delta_i^n)$, the rows of the 2×3 Jacobian $D\boldsymbol{\delta}_i(q_0)$ are the differentials $D\delta_i^t(q_0)$ and $D\delta_i^n(q_0)$. Since $\frac{d}{dt}\delta_i^t(q(t)) = t_i \cdot G_i(q(t))\dot{q}$ according to (2), $D\delta_i^t = t_i^T G_i$. Similarly, it can be verified that $\frac{d}{dt}\delta_i^n(q(t)) = -n_i \cdot G_i(q(t))\dot{q}$ [31], and consequently $D\delta_i^n = -n_i^T G_i$.[2] The formula for $D\boldsymbol{\delta}_i(q_0)$ is thus $D\boldsymbol{\delta}_i(q_0) = \begin{bmatrix} t_i^T \\ -n_i^T \end{bmatrix} G_i(q_0)$. Substituting for $K_i(q_0)$ and $D\boldsymbol{\delta}_i(q_0)$ in the product $K_i(q_0)D\boldsymbol{\delta}_i(q_0)$ gives

$$\begin{aligned} K_i(q_0)D\boldsymbol{\delta}_i(q_0) &= \begin{bmatrix} -\frac{4}{3(2-\nu)} & -\frac{2c_i}{3(2-\nu)} \\ 0 & \frac{1}{1-\nu} \end{bmatrix} \begin{bmatrix} t_i^T \\ -n_i^T \end{bmatrix} G_i(q_0) \\ &= -\begin{bmatrix} \frac{4}{3(2-\nu)} & -\frac{2c_i}{3(2-\nu)} \\ 0 & \frac{1}{1-\nu} \end{bmatrix} \begin{bmatrix} t_i^T \\ n_i^T \end{bmatrix} G_i(q_0) \\ &= -\begin{bmatrix} \frac{4}{3(2-\nu)} & -\frac{2c_i}{3(2-\nu)} \\ 0 & \frac{1}{1-\nu} \end{bmatrix} R_i^T(q_0)G_i(q_0), \end{aligned}$$

where we omitted the scalars preceding $K_i(q_0)$ and substituted $R_i^T = \begin{bmatrix} t_i^T \\ n_i^T \end{bmatrix}$. Pre-multiplying the latter expression by $G_i^T(q_0)R_i(q_0)$ gives the formula for $\tilde{K}_i(q_0)$. □

In preparation for the grasp stability analysis conducted in the next section, we need to establish when the symmetric part of $\tilde{K}_i$, $(\tilde{K}_i)_s = \frac{1}{2}\left(\tilde{K}_i + \tilde{K}_i^T\right)$, is negative semi-definite. A key result is that the negative semi-definiteness of $(\tilde{K}_i)_s$ depends solely on the slope of the linear loading profile.

[2] The contact normal n_i points into $\mathcal{B}$ and $\dot{x}_i = G_i\dot{q}$. Hence $\frac{d}{dt}\delta_i^n(q(t)) = (-n_i) \cdot \dot{x}_i > 0$ means that $\mathcal{B}$ penetrates deeper into $\mathcal{A}_i$, while the converse holds when $\frac{d}{dt}\delta_i^n(q(t)) < 0$.

Proposition 3.2. *Let the i^{th} contact be loaded along a linear loading profile with slope c_i. If the loading profile satisfies the inequality*

$$|c_i| < 2\sqrt{\frac{3(2-\nu)}{(1-\nu)}}, \tag{8}$$

the symmetrized stiffness matrix induced by the i^{th} contact, $\left(\tilde{K}_i(q_0)\right)_s$, is **negative semi-definite.**

Proof: Denote by A_i the 2×2 matrix at the core of $\tilde{K}_i(q_0)$ in (7):

$$A_i = \begin{bmatrix} \frac{4}{3(2-\nu)} & -\frac{2c_i}{3(2-\nu)} \\ 0 & \frac{1}{1-\nu} \end{bmatrix}.$$

Then $(\tilde{K}_i)_s = -G_i^T R_i (A_i)_s R_i^T G_i$, where we omitted the positive scalars preceding $\tilde{K}_i$. The positive definiteness of $(A_i)_s$ implies the negative semi-definiteness of $(\tilde{K}_i)_s$. The 2×2 matrix $(A_i)_s$ is positive definite when its two eigenvalues, λ_1 and λ_2, are strictly positive. First consider the trace of $(A_i)_s$, $\mathsf{tr}(A_i)_s = \lambda_1 + \lambda_2$. Inspection of the diagonal elements in $(A_i)_s$ reveals that $\mathsf{tr}(A_i)_s > 0$ when $\nu < 1$. Since Poisson's ratio satisfies $0 \leq \nu \leq 0.5$ for all practical materials, $\mathsf{tr}(A_i)_s > 0$. Next consider the determinant of $(A_i)_s$, $\det(A_i)_s = \lambda_1 \lambda_2$. Since $\lambda_1 + \lambda_2 > 0$, a positive determinant would imply positive definiteness of $(A_i)_s$. The determinant of $(A_i)_s$ is:

$$\det(A_i)_s = \frac{4}{3(1-\nu)(2-\nu)} - \frac{c_i^2}{9(2-\nu)^2}.$$

The inequality $\det(A_i)_s > 0$ becomes $4/(1-\nu) > c_i^2/3(2-\nu)$. A square root of both sides gives the condition for the positive definiteness of $(A_i)_s$, which implies the negative semi-definiteness of $(\tilde{K}_i)_s$. □

Example: Consider the constraint imposed on $|c_i|$ by (8). Since $0 \leq \nu \leq 0.5$, the term $(2–\nu)/(1–\nu)$ varies in the interval $[2, 3]$. Hence $(\tilde{K}_i)_s$ is negative semi-definite when $|c_i| < 2\sqrt{6}$. The corresponding slope angle of the linear loading profile, denoted ψ in Figure 3, must satisfy $|\psi| < 78.5°$. The slope of the linear loading profile must also satisfy the friction cone constraint specified in (3), $|c_i| < \mu(2-\nu)/2(1-\nu)$. Since $(2-\nu)/2(1-\nu)$ varies in the interval $[1, 3/2]$, the friction cone constraint is satisfied when $|c_i| < \mu$. The linear loading path must always satisfy the friction cone constrain. The negative semi-definiteness of $(\tilde{K}_i)_s$ is therefore automatic as long as $\mu \leq 2\sqrt{6}$, which clearly holds true in most practical situations. For instance, when $\mu = 1$ the linear loading slope angle, denoted ϕ in Figure 3, must satisfy $|\phi| < 45°$, which is well within the $78.5°$ constraint imposed by (8). The matrix $(\tilde{K}_i)_s$ is thus negative semi-definite in typical linearly loaded grasps.

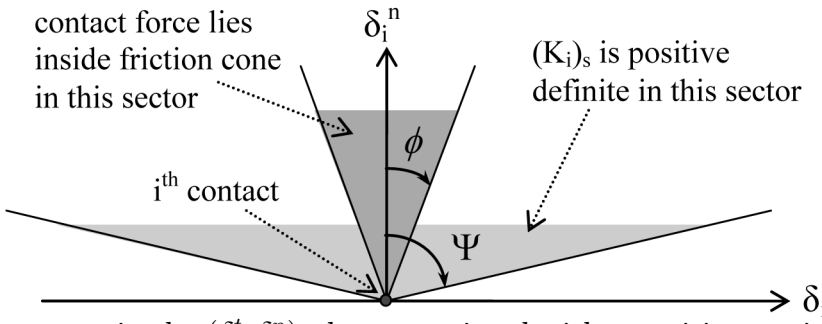

Figure 3: The sectors in the (δ_i^t, δ_i^n)-plane associated with a positive semi-definite $(\tilde{K}_i)_s$ and the friction cone constraint. Typically $|\phi| < 45°$ while $|\psi| < 78.5°$.

4 Grasp Stiffness and Stability Analysis

Based on the wrench-displacement relationship affected on $\mathcal{B}$ by the individual contacts satisfying the Hertz-Walton compliance model, this section characterizes the stiffness and stability of multi-contact grasps. Section 4.1 derives the linearized dynamics of $\mathcal{B}$ at a multi-contact equilibrium grasp. The resulting grasp dynamics is governed by an asymmetric grasp stiffness matrix. Section 4.2 introduces a generic stability criterion for asymmetric linear systems [33]. Based on this criterion, we obtain the conditions under which $\mathcal{B}$ is stably held by the compliant contacts.

4.1 Linearized Grasp Dynamics

Let the object $\mathcal{B}$ be held in equilibrium grasp by stationary finger bodies $\mathcal{A}_1, \ldots, \mathcal{A}_k$. The bodies are assumed to lie on a frictionless plane such that the inter-body forces are parallel to this plane. The undeformed bodies are assumed to have spherical surfaces at the contacts, and the contacts are assumed to be preloaded along linear loading profiles in accordance with the Hertz-Walton model. The wrench induced on $\mathcal{B}$ by a contact force $f_i(q, \dot{q})$ acting at x_i is given by $G_i^T(q) f_i(q, \dot{q})$, where $G_i = DX_{r_i}(q)$ is the Jacobian of $X_{r_i}(q)$. The dynamics of $\mathcal{B}$ within the planar environment under the influence of k contact forces, without any other external influences, is given by

$$M(q)\ddot{q} + C(q, \dot{q}) = \sum_{i=1}^{k} G_i^T(q) f_i(q, \dot{q}), \tag{9}$$

where $M(q)$ is $\mathcal{B}$'s 3×3 inertia matrix, and $C(q, \dot{q})$ is the vector of centrifugal and Coriolis forces acting on $\mathcal{B}$. As before, q_0 denotes the object's equilibrium configuration. To determine the linearized dynamics of $\mathcal{B}$ at $(q, \dot{q}) = (q_0, 0)$, denote by $(p_1, p_2) = (q, \dot{q})$ the state variables

of $\mathcal{B}$. Then (9) can be written as

$$\begin{aligned} \dot{p}_1 &= p_2 \\ \dot{p}_2 &= M^{-1}(p_1)\big(\textstyle\sum_{i=1}^{k} G_i^T(p_1) f_i(p_1, p_2) - C(p_1, p_2)\big). \end{aligned} \tag{10}$$

The following proposition describes the linearized dynamics of $\mathcal{B}$ at $(q_0, 0)$ (see appendix for a proof of the proposition).

Proposition 4.1. *Let a quasi-rigid body $\mathcal{B}$ be held at an equilibrium grasp configuration, $q_0 = (d_0, \theta_0)$, by quasi-rigid bodies $\mathcal{A}_1, \ldots, \mathcal{A}_k$. Let $\Delta p_1 = q - q_0$ and $\Delta p_2 = \dot{q} - 0$. The* **linearized dynamics** *of $\mathcal{B}$ at $(q_0, 0)$ is given by*

$$\frac{d}{dt}\begin{pmatrix}\Delta p_1 \\ \Delta p_2\end{pmatrix} = \begin{bmatrix} O_{3\times 3} & I_{3\times 3} \\ -M^{-1}(q_0)K_p(q_0, 0) & -M^{-1}(q_0)K_d(q_0, 0)\end{bmatrix}\begin{pmatrix}\Delta p_1 \\ \Delta p_2\end{pmatrix}, \tag{11}$$

where K_p and K_d are the grasp stiffness and damping matrices. The grasp stiffness matrix is the **asymmetric** *3×3 matrix:*

$$K_p(q_0, 0) = -\sum_{i=1}^{k}\left\{\tilde{K}_i(q_0) - \begin{bmatrix} O_{2\times 2} & 0 \\ 0^T & \boldsymbol{\rho}_i(\theta_0)\cdot f_i \end{bmatrix} + G_i^T(q_0)\begin{bmatrix} f_i^n & f_i^t \\ -f_i^t & f_i^n \end{bmatrix} Dn_i(q_0)\right\}, \tag{12}$$

where $\tilde{K}_i(q_0)$ is the i^{th} contact c-space stiffness matrix, $\boldsymbol{\rho}_i(\theta_0)$ is the i^{th} contact position relative to $\mathcal{B}$'s origin, f_i is the i^{th} contact force with components (f_i^t, f_i^n), and n_i is the i^{th} contact normal $(i = 1 \ldots k)$. The grasp damping matrix is the symmetric 3×3 matrix:

$$K_d(q_0, 0) = \sum_{i=1}^{k} \delta_i^n(q_0) G_i^T(q_0) R_i(q_0) \begin{bmatrix} \frac{\partial \varphi_i^t}{\partial \dot{\delta}_i^t}(0) & 0 \\ 0 & \frac{\partial \varphi_i^n}{\partial \dot{\delta}_i^n}(0) \end{bmatrix} R_i^T(q_0) G_i(q_0), \tag{13}$$

where φ_i^t and φ_i^n are the tangential and normal damping functions at the i^{th} contact $(i = 1 \ldots k)$.

Let us discuss the three terms appearing in the stiffness matrix K_p. The first term, $-\sum_{i=1}^{k}\tilde{K}_i$, is the net wrench generated by the compliant contacts on $\mathcal{B}$. This term forms an asymmetric matrix under the Hertz-Walton compliance model. As a result, the linearized grasp dynamics is *not* governed by any potential energy function. The second term, $\sum_{i=1}^{k}\boldsymbol{\rho}_i \cdot f_i$, represents the effect of the preload forces on the grasp stiffness matrix. When the preload level is too high this term can possibly destabilize the grasp, a phenomena known as "coin snapping" in the grasping literature [5, 21, 26]. The third term represents the overlap-segment change

of direction due to small displacements of $\mathcal{B}$. This term depends on the curvatures of the undeformed bodies. As shown in Ref. [21], the 2×3 Jacobian Dn_i is given by

$$Dn_i(q_0) = \frac{1}{r_{\mathcal{A}_i} + r_{\mathcal{B}_i} - \delta_i^n(q_0)} \left[I - n_i n_i^T,\ (r_{\mathcal{B}_i} + \boldsymbol{\rho}_i(\theta_0) \cdot n_i) J n_i \right], \tag{14}$$

where I is a 2×2 identity matrix, $J = \begin{bmatrix} 0 & -1 \\ 1 & 0 \end{bmatrix}$, and $r_{\mathcal{A}_i}$ and $r_{\mathcal{B}_i}$ are the radii of curvature of $\mathcal{A}_i$ and $\mathcal{B}$ at the endpoints of the i^{th} overlap segment. The curvature term in K_p also depends on the preload force components, (f_i^t, f_i^n) for $i = 1 \ldots k$. Therefore, when curvature effects have a stabilizing influence their influence becomes more pronounced with higher preload levels (see Section 5). Finally, the damping matrix, K_d, is proportional to the normal penetration, δ_i^n, which is strictly positive at a preloaded contact. Since the damping functions φ_i^t and φ_i^n are monotonically increasing in their respective arguments, K_d is a symmetric positive semi-definite matrix.

We will analyze the equilibrium grasp stability based on a generic stability criterion for asymmetric second-order linear systems. To apply this criterion, we write the linearized grasp dynamics (11) in the standard form:

$$M(q_0)\Delta\ddot{q} + K_d(q_0, 0)\Delta\dot{q} + K_p(q_0, 0)\Delta q = \vec{0}, \tag{15}$$

where $\Delta q = q - q_0$ and $\Delta\dot{q} = \dot{q} - 0$. Note that $M(q_0)$ and $K_d(q_0, 0)$ are symmetric positive definite matrices while $K_p(q_0, 0)$ is an asymmetric matrix.

4.2 Stability of Second-Order Asymmetric Linear Systems

The local stability of a compliant equilibrium grasp can be generically determined from its linearized dynamics at the equilibrium grasp. When the contacts are governed by the Hertz-Walton compliance law, the linearized grasp dynamics forms an asymmetric second-order linear system (Proposition 4.1). The stability of such systems can be determined as follows. Given an $n \times n$ matrix A, its symmetric and asymmetric parts are given by $A_s = \frac{1}{2}(A + A^T)$ and $A_{as} = \frac{1}{2}(A - A^T)$, while its norm is given by $\|A\| = \max_{\|v\| \leq 1}\{\|Av\|\}$ for $v \in I\!R^n$. When A is a symmetric matrix, its minimal eigenvalue is denoted $\lambda_{min}(A)$. The following theorem describes a generic criterion for the stability of asymmetric second-order linear systems.

Theorem 1 ([33]). *Consider the second-order linear system in the variable $p \in I\!R^n$,*

$$M\ddot{p} + K_d\dot{p} + K_p p = \vec{0}, \tag{16}$$

where $M \in I\!R^{n \times n}$ and $K_d \in I\!R^{n \times n}$ are symmetric positive definite matrices, while $K_p \in I\!R^{n \times n}$ is an asymmetric matrix such that $(K_p)_s$ is positive definite. Let $\alpha > 0$ be the minimal

eigenvalue of $M^{-1/2}(K_p)_s M^{-1/2}$*, let* $\beta > 0$ *be the minimal eigenvalue of* $M^{-1/2}K_d M^{-1/2}$*, and let* $\gamma \geq 0$ *be the matrix norm of* $M^{-1/2}(K_p)_{as}M^{-1/2}$*. If* α*,* β*, and* γ *satisfy the relation:*

$$\gamma < \sqrt{\alpha}\beta$$

the system (16) is **globally asymptotically stable.**

The condition $\gamma < \sqrt{\alpha}\beta$ can be interpreted as follows. Consider the case where M is an identity matrix. Then $\alpha = \lambda_{min}\big((K_p)_s\big)$, $\beta = \lambda_{min}(K_d)$, and the condition $\gamma < \sqrt{\alpha}\beta$ becomes:

$$\|(K_p)_{as}\| < \lambda_{min}(K_d)\sqrt{\lambda_{min}\big((K_p)_s\big)}.$$

The stability condition essentially requires that the asymmetric part of K_p be sufficiently small relative to the symmetric part of K_p (which is modulated by the damping $\lambda_{min}(K_d)$). The following numerical example illustrates the applicability of the stability criterion.

Example: Consider the asymmetric second-order linear system:

$$\begin{bmatrix} 10 & 0 \\ 0 & 11 \end{bmatrix} \ddot{p} + \begin{bmatrix} 4 & 1 \\ 1 & 5 \end{bmatrix} \dot{p} + \begin{bmatrix} 8 & s \\ -s & 9 \end{bmatrix} p = 0, \tag{17}$$

where s is a free parameter. The matrices M, K_d, and $(K_p)_s$ are all symmetric positive definite. Hence, when $s = 0$ the system is symmetric and asymptotically stable. Qualitatively, increasing the value of s increases the asymmetric part of the stiffness matrix. Calculation of α, β, and γ yields $\alpha = 4/5$, $\beta = 0.328$, and $\gamma = s/\sqrt{110}$. Therefore, the stability condition of Theorem 1 becomes the condition $|s| < 3.078$. For comparison we numerically calculated the eigenvalues of the 4×4 matrix $\begin{bmatrix} O & I \\ K_p & K_d \end{bmatrix}$. It turns out that for $0 \leq s < 3.920$ the system (17) is asymptotically stable. Thus, apart from being conservative, the stability condition (16) correctly predicts the system's global asymptotic stability.

The following key theorem applies the generic stability criterion, $\gamma < \sqrt{\alpha}\beta$, to the linearized grasp dynamics.

Theorem 2 (Compliant Grasp Stability)**.** *Let a quasi-rigid body* $\mathcal{B}$ *be grasped at an equilibrium* q_0 *by quasi-rigid bodies* $\mathcal{A}_1, \ldots, \mathcal{A}_k$ *satisfying the Hertz-Walton compliance law. Define the scalars* α*,* β*, and* γ *as*

$$\begin{aligned} \alpha &= \lambda_{min}\left(M^{-\frac{1}{2}}(q_0)(K_p(q_0,0))_s M^{-\frac{1}{2}}(q_0)\right) \\ \beta &= \lambda_{min}\left(M^{-\frac{1}{2}}(q_0)K_d(q_0,0)M^{-\frac{1}{2}}(q_0)\right) \\ \gamma &= \|M^{-\frac{1}{2}}(q_0)(K_p(q_0,0))_{as}M^{-\frac{1}{2}}(q_0)\|, \end{aligned}$$

where $M(q_0)$ is $\mathcal{B}$'s inertia matrix, $K_p(q_0,0)$ is the grasp's stiffness matrix, and $K_d(q_0,0)$ is the grasp's damping matrix.
If $\alpha > 0$, $\beta > 0$, and $\gamma < \sqrt{\alpha}\beta$, the zero-velocity state $(q_0,0)$ of the nonlinear grasp dynamics (9) is **locally asymptotically stable.**

Proof: A nonlinear system $\dot{x} = F(x)$ has a *hyperbolic* equilibrium at x_0 when $F(x_0) = \vec{0}$ and the Jacobian $DF(x_0)$ has eigenvalues with non-zero real part [13]. When the system $\dot{x} = F(x)$ has a hyperbolic equilibrium at x_0, the system's local stability is fully determined by its linearized dynamics at x_0, a result known as the Hartman-Grobman lemma [11]. The linearized grasp dynamics at $(q_0,0)$ has the form (see eq. (15)):

$$M(q_0)\Delta\ddot{q} + K_d(q_0)\Delta\dot{q} + K_p(q_0)\Delta q = 0. \tag{18}$$

Based on Theorem 1, the conditions $\alpha > 0$, $\beta > 0$, and $\gamma < \sqrt{\alpha}\beta$, ensure the global asymptotically stability of the linear system (18). Since an asymptotically stable equilibrium is necessarily hyperbolic, the nonlinear grasp dynamics is locally asymptotically stable. □

5 Synthesis of Compliantly Stable Grasps

This section suggests practical guidelines for synthesizing compliantly stable grasps based on the stability criterion of Theorem 2. To synthesize a compliantly stable grasp, one must satisfy the three conditions $\alpha > 0$, $\beta > 0$, and $\gamma < \sqrt{\alpha}\beta$. To simplify the discussion, assume the object $\mathcal{B}$ is grasped along planar facets perpendicular to the supporting plane. In this case the grasp stiffness matrix, K_p, has the following simple form (see appendix for a proof of the lemma).

Lemma 5.1. *When $\mathcal{B}$ is held in equilibrium grasp along planar facets, the grasp stiffness matrix specified in eq. (12) becomes*

$$K_p(q_0,0) = -\sum_{i=1}^{k} \tilde{K}_i(q_0), \tag{19}$$

where $\tilde{K}_i(q_0)$ is the i^{th} c-space contact stiffness matrix for $i = 1 \ldots k$.

As shown in the proof of the lemma, when $\mathcal{B}$ is held along planar facets curvature effects contribute a stabilizing term to K_p. (This stabilizing effect can be intuitively observed by holding a coin along its flat facets with two fingers; the coin remains stably held by the two fingers even when the preload forces increase.) The stabilizing curvature term cancels the

term proportional to the preload forces in (12), and the resulting K_p depends solely on the contact stiffness matrices.

The $\alpha > 0$ condition: Since $\alpha = \lambda_{min}(M^{-1/2}(K_p)_s M^{-1/2})$ and $M^{-1/2}$ is non-singular, the condition $\alpha > 0$ is equivalent to the condition $\lambda_{min}\big((K_p)_s\big) > 0$. The symmetric part of K_p is given by

$$(K_p(q_0, 0))_s = -\sum_{i=1}^{k} \big(\tilde{K}_i(q_0)\big)_s.$$

According to Proposition 3.2, each $(\tilde{K}_i)_s$ is negative semi-definite when the slope of the linear loading profile slope, c_i, satisfies a mild requirement which is automatically maintained for friction coefficients in the range $\mu \leq 2\sqrt{6}$. For these friction coefficients $(K_p)_s$ is positive definite based on the following argument. According to Lemma 3.1, each $(\tilde{K}_i)_s$ is given by

$$\big(\tilde{K}_i(q_0)\big)_s = -\sqrt{\delta_i^n(q_0)} G_i^T(q_0) R_i(q_0) \begin{bmatrix} \frac{4}{3(2-\nu)} & -\frac{2c_i}{3(2-\nu)} \\ 0 & \frac{1}{1-\nu} \end{bmatrix}_s R_i^T(q_0) G_i(q_0), \tag{20}$$

where we omitted the positive scalars $4G\sqrt{r_i}$ from the formula (in particular, $r_i = 1$ when $\mathcal{B}$ is held along planar facets). Since $G_i(q_0) = DX_{r_i}$, the kernel of $\big(\tilde{K}_i\big)_s$ occurs along instantaneous motions of $\mathcal{B}$ satisfying $DX_{r_i}\dot{q} = \dot{x}_i = \vec{0}$, where x_i is the i^{th} contact. Such motions correspond to instantaneous rolling of $\mathcal{B}$ about x_i. Since $\mathcal{B}$ cannot instantaneously roll about all k contacts, the matrix $(K_p)_s = -\sum_{i=1}^{k}(\tilde{K}_i)_s$ is positive definite (and hence $\alpha > 0$) for reasonable friction coefficients.

The $\beta > 0$ condition: Since $\beta = \lambda_{min}(M^{-1/2} K_d M^{-1/2})$ and $M^{-1/2}$ is non-singular, the condition $\beta > 0$ is equivalent to the condition $\lambda_{min}(K_d) > 0$. The damping matrix is given by

$$K_d(q_0, 0) = \sum_{i=1}^{k} \delta_i^n(q_0) G_i^T(q_0) R_i(q_0) \begin{bmatrix} \frac{\partial \varphi_i^t}{\partial \dot{\delta}_i^t}(0) & 0 \\ 0 & \frac{\partial \varphi_i^n}{\partial \dot{\delta}_i^n}(0) \end{bmatrix} R_i^T(q_0) G_i(q_0),$$

where $\varphi_i^t(\dot{\delta}_i^t)$ and $\varphi_i^n(\dot{\delta}_i^n)$ are the damping functions at the i^{th} contact. The damping functions are monotonically increasing in their respective arguments, hence $\frac{\partial \varphi_i^t}{\partial \dot{\delta}_i^t}(0)$ and $\frac{\partial \varphi_i^n}{\partial \dot{\delta}_i^n}(0)$ are strictly positive. Since $\delta_i^n(q_0) > 0$ for $i = 1 \ldots k$ and $\mathcal{B}$ cannot instantaneously roll about all k contacts, the matrix K_d is automatically positive definite and hence $\beta > 0$.

While K_d is positive definite, its exact value depends on intricate damping processes. For instance, small movements of $\mathcal{B}$ induce frictional micro-slip within the contact regions. Damping is also induced by viscoelastic effects within the compressed material (e.g. [9][177-182],[19][242-247]). The modeling of damping in compliant grasps is under investigation by

several research groups [37, 38, 39]. Until such models become available, we lump the net effect of damping by a positive scalar, $\kappa_d = \lambda_{min}(M^{-1/2} K_d M^{-1/2}) > 0$.

The $\gamma < \sqrt{\alpha}\beta$ condition: Since $\alpha = \lambda_{min}\big((K_p)_s\big)$ and $\gamma = \|M^{-1/2}(K_p)_{as}M^{-1/2}\|$, the condition $\gamma < \sqrt{\alpha}\beta$ is given by

$$\|M^{-\frac{1}{2}}\big(K_p(q_0,0)\big)_{as}M^{-\frac{1}{2}}\| < \kappa_d\sqrt{\lambda_{min}(M^{-\frac{1}{2}}\big(K_p(q_0,0)\big)_s M^{-\frac{1}{2}})}. \tag{21}$$

Let us show that (21) limits the allowed linear loading profiles to particular sectors centered on the contact normals. We first scale the c-space coordinates by the grasp's characteristic length (this scaling essentially normalizes $\mathcal{B}$'s orientation coordinate relative to its translation coordinates). Let the grasp's *centroid* be the average contact position: $x_c = \frac{1}{k}\sum_{i=1}^{k} x_i$, where $x_1, \ldots, x_k$ are the contact locations. The grasp's *characteristic length* is the mean squared distance of the contacts from x_c:

$$l_c = \sqrt{\frac{1}{k}\sum_{i=1}^{k}\|x_i - x_c\|^2}.$$

The parameter l_c induces the following scaling of $\mathcal{B}$'s c-space coordinates

$$q = S\bar{q} \quad \text{where} \quad S = \begin{bmatrix} I_{2\times 2} & 0 \\ 0^T & 1/l_c \end{bmatrix}.$$

The grasp's stiffness matrix and $\mathcal{B}$'s inertia matrix are given in the $\bar{q}$ coordinates by

$$\bar{K}_p(\bar{q}_0, 0) = S^T K_p(q_0, 0) S \quad \text{and} \quad \bar{M}(\bar{q}_0) = S^T M(q_0) S,$$

where $q_0 = S\bar{q}_0$. Condition (21) is specified in the $\bar{q}$ coordinates by

$$\|\bar{M}^{-\frac{1}{2}}\big(\bar{K}_p(\bar{q}_0,0)\big)_{as}\bar{M}^{-\frac{1}{2}}\| < \kappa_d\sqrt{\lambda_{min}(\bar{M}^{-\frac{1}{2}}\big(\bar{K}_p(\bar{q}_0,0)\big)_s \bar{M}^{-\frac{1}{2}})}. \tag{22}$$

In order to proceed with the assessment of (22), let us approximate the normal penetration at the contacts, $\delta_i^n(q_0)$ for $i = 1 \ldots k$, by a characteristic normal penetration, $\delta_i^n(q_0) \cong \delta_c^n$ for $i = 1 \ldots k$. Let us also approximate the loading profile slopes, c_i for $i = 1 \ldots k$, by a characteristic slope parameter, $c \cong c_i$ for $i = 1 \ldots k$. When these approximations are substituted into the matrices $\tilde{K}_i$ for $i = 1 \ldots k$, the symmetric and asymmetric parts of $\bar{K}_p = -\sum_{i=1}^{k} S^T \tilde{K}_i S$ are given by

$$\big(\bar{K}_p(\bar{q}_0,0)\big)_s \cong \sqrt{\delta_c^n}\sum_{i=1}^{k} S^T G_i^T R_i A_s R_i^T G_i S \tag{23}$$

and

$$\left(\bar{K}_p(\bar{q}_0,0)\right)_{as} \cong \sqrt{\delta_c^n}\sum_{i=1}^{k} S^T G_i^T R_i A_{as} R_i^T G_i S, \tag{24}$$

where A_s and A_{as} are the symmetric and asymmetric parts of the 2×2 matrix:

$$A = \begin{bmatrix} \frac{4}{3(2-\nu)} & -\frac{2c}{3(2-\nu)} \\ 0 & \frac{1}{1-\nu} \end{bmatrix}. \tag{25}$$

The matrix A represents the contact stiffness matrices, where c is the slope of the linear loading profiles. The following proposition asserts that the condition $\gamma < \sqrt{\alpha}\beta$ essentially requires that A_{as} be sufficiently small relative to A_s (see appendix for a proof of the proposition).

Proposition 5.2. *Let $\mathcal{B}$ be held along planar facets in a k-finger grasp, such that $\delta_i^n(q_0) \cong \delta_c^n$ and $c_i \cong c$ for $i = 1 \ldots k$. Let $\alpha > 0$ and $\beta > 0$ for the given grasp. The condition $\gamma < \sqrt{\alpha}\beta$ is satisfied when A_s and A_{as} satisfy the condition:*

$$\|A_{as}\| < \kappa_d \frac{\lambda_{min}(\bar{M})}{\lambda_{max}(\bar{M})}\sqrt{\lambda_{min}(A_s)}, \tag{26}$$

where A is specified in (25), κ_d is the damping parameter, and $\bar{M}$ is $\mathcal{B}$'s scaled inertia matrix.

The symmetric and asymmetric parts of A are given by

$$A_s = \begin{bmatrix} a(\nu) & -\frac{c}{3(2-\nu)} \\ -\frac{c}{3(2-\nu)} & b(\nu) \end{bmatrix} \quad \text{and} \quad A_{as} = \begin{bmatrix} 0 & -\frac{c}{3(2-\nu)} \\ \frac{c}{3(2-\nu)} & 0 \end{bmatrix},$$

where c is the slope of the linear loading profile, $a(\nu) = 4/3(2-\nu)$, and $b(\nu) = 1/1-\nu$. The norm of A_{as} is given by $\|A_{as}\| = |c|/3(2-\nu)$, while the minimal eigenvalue of A_s satisfies the inequality $\lambda_{min}(A_s) \geq \det(A_s)/\mathsf{tr}(A_s)$.[3] Substituting for the determinant and trace of A_s, condition (26) is implied by the stricter inequality:

$$\frac{|c|}{3(2-\nu)} < \kappa_d \frac{\lambda_{min}(\bar{M})}{\lambda_{max}(\bar{M})}\left(\frac{a(\nu)b(\nu) - \frac{c^2}{9(2-\nu)^2}}{a(\nu)+b(\nu)}\right)^{\frac{1}{2}}. \tag{27}$$

Note that $\det(A_s)$ and $\mathsf{tr}(A_s)$ are strictly positive in (27) (since $\alpha = \lambda_{min}(A_s) > 0$), hence the square root in (27) is well defined. After some algebraic manipulation, (27) can be written as the following constraint on the linear loading profile slope:

$$|c| < 3\kappa\left(\frac{a(\nu)b(\nu)}{a(\nu)+b(\nu)+\kappa^2}\right)^{\frac{1}{2}}(2-\nu) \qquad \text{where } \kappa = \kappa_d\frac{\lambda_{min}(\bar{M})}{\lambda_{max}(\bar{M})}. \tag{28}$$

[3] If λ_1 and λ_2 are A_s's minimal and maximal eigenvalues (both positive), $\det(A_s)/\mathsf{tr}(A_s) = \lambda_1\lambda_2/(\lambda_1+\lambda_2) \leq \lambda_1$.

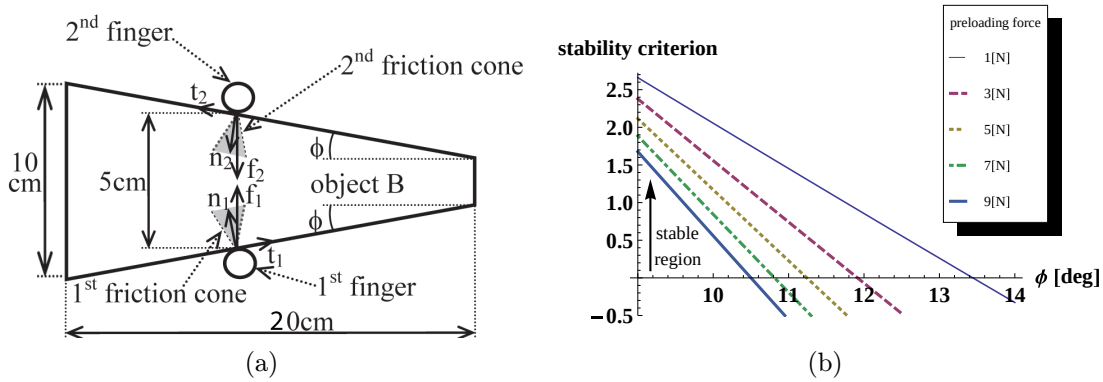

Figure 4: A two-finger grasp of a family of wedge-like objects: (a) the system's schema; (b) criterion computation.

Grasp stability is thus ensured when the contacts are loaded with linear loading profiles which lie in the sectors specified by (28). One is thus lead to the following qualitative guidlines for ensuring grasp stability (the precise stability can be evaluated with the formulas of Theorem 2). As the allowed sectors are centered on the contact normals (corresponding to $c = 0$), one should ideally select contact locations at which the equilibrium grasp can be preloaded along the contact normals. When such contact locations are infeasible, one should select contact locations at which the feasible linear loading profiles are *as close as possible* to the contact normal directions. If the contact locations are pre-determined by other task constraints, align the linear loading profiles *as close as possible* to the contact normals within the allowed friction cone, as these directions will maximize the grasp stability margin with respect to small errors in the loading profile directions. These qualitative considerations are illustrated with the following numerical examples.

Example – a two-fingered grasp of a wedge–like object: Consider the wedge-like object shown in Figure 4(a). The object is held by two spherical fingers along planar facet in a frictional equilibrium grasp. The object's width is 20 cm, its hight at the contacts is 5 cm, and its thickness is 10 cm. The object's head angle is ϕ and base angle is $90°$–ϕ. When ϕ varies as a free parameter, this example represents a family of wedge-like objects with different head angles. The friction coefficient is assumed sufficiently large so that the fingers do not slide. When material compliance is taken into account, the grasp stiffness matrix K_p is asymmetric and local deformations at the contacts may cause instability. When the finger preload forces, f_1 and f_2, are aligned with the contact normals K_p is perfectly symmetric and in this case $\|(K_p)_{as}\| = 0$. However, equilibrium feasibility requires that the finger forces be collinear

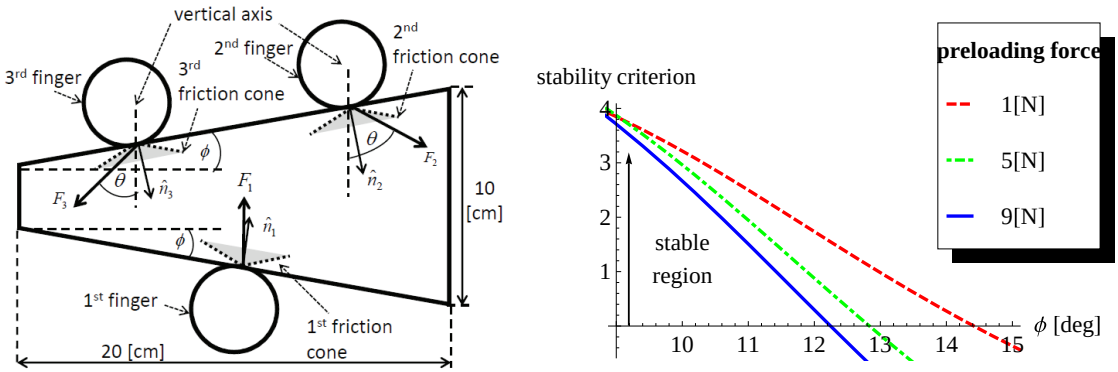

(a) (b)

Figure 5: A Three-finger grasp of a family of wedge-like objects: (a) the system's schema; (b) criterion computation – preloading force refer to finger 1.

with opposite directions. As the object's head angle ϕ increases, the finger forces must rotate away from the normal directions in order to maintain the equilibrium grasp. During this rotation $\|(K_p)_{as}\|$ increases and the margin of stability specified in Proposition 5.2 becomes less favorable. The stability condition (26) places a limit on the allowed rotation and consequently bounds the maximal allowed angle ϕ. As expected, stronger grasp forces lead to reduction of the maximal ϕ value, that assure the system's stability -Figure 4(b). For example, considering: Aluminum material properties, preload of $9[N]$ in each finger, and maintaining $\gamma < \sqrt{\alpha}\beta$ (hence the grasp is stable), yields that the range of ϕ which assures stability is $\phi \leq 10.50°$.

Example – a three-fingered grasp of a wedge–like object: Analysing a three fingered grasp of the same wedge–like object, is done in a similar manner to the previous example. In the 3-finger case, as depicted in Figure 5(a), finger 1 apply a vertical force and fingers 2 and 3 apply an oblique loading such that their horizontal part cancel each other. Therefore, these two forces are constrained to be of the same magnitude, and their directions with respect to the vertical line is the angle θ. The same properties are taken: Aluminum material properties, and maintaining $\gamma < \sqrt{\alpha}\beta$ (hence the grasp is stable). As in the previous example, increasing the grasping forces reduces ϕ's range where the system is stable.

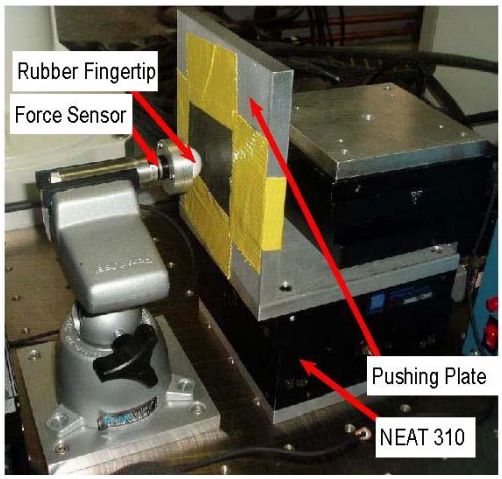

Figure 6: Experimental setup showing the compliant material, a gum rubber, mounted to a static force sensor which is clamped to an experimental table. A two-axis displacement device NEAT 310 drives the pushing plate into the compliant material.

6 Experiments and Results

The purpose of the experiments is to determine how effectively the simple lumped parameter Hertz-Walton model can be used to predict contact forces. In this section we wish to fit the experimental force-displacement data to following parametric model:

$$\begin{bmatrix} f_n \\ f_t \end{bmatrix} = \begin{bmatrix} k_n \delta_n^{\frac{3}{2}} \\ \frac{k_t}{\sqrt{c}} \delta_t^{\frac{3}{2}} \end{bmatrix} \tag{29}$$

where c is the deflection ratio $c = \frac{\delta_t}{\delta_n}$, and k_n, k_t are constants that lump the material and geometric properties of the contacting bodies. In particular, we would like the model to be valid for a variety of loading paths, including normal loading paths, linear loading paths, and some range of non-linear loading paths as well.

6.1 Experimental Setup

The three main components of our experimental setup, required to generate force-displacement data, are a high precision displacement device, a force sensor, and the compliant material. The overall setup is shown in Figure 6.

We utilized the NEAT-310, produced by New England Affiliated Technologies, as a high precision displacement devise. The NEAT-310 consists of a two axis output stage, with each

axis individually driven by a $1[\mu m]$ resolution stepper motor. The force sensor we used was the Nano17 6-axis force-torque sensor by ATI Industrial Automation. The force resolution of the device is $\frac{1}{1280}[N]$ on each force axis and is rated up to $50[N]$. The compliant material we chose to experiment on was a pure gum rubber ball available from McMaster-Carr as part number 96385K62. This material was chosen primary for its compliance properties, which rates it as a 45-50 on the Shore A scale[4]. The material is sold as a 1" diameter ball. The main advantage of using such a compliant material is that the compliance of the rest of the system (i.e. force sensor and structural compliance) is negligible with respect to the compliance of the rubber ball.

In order to setup the three main components, the compliant material was cut in half to make a half-sphere, and mounted onto a plate which attached to the force sensor. The force sensor was screwed to an aluminum tube, which was clamped and then the clamp was screwed to an experimental table. This setup held the compliant material fixed with respect to the experimental table. The NEAT-310 stage was also screwed to the experimental table. A vertical aluminum plate was attached to the device's output stage. This vertical plate, covered with sandpaper to increase contact friction, served as the pushing surface to compress the complaint material. See Figure 6.

6.2 Normal Loading Path Experiments

Ten normal loading experiments were conducted, each of which loaded the compliant material to 25 [N] in the normal direction. The normal component of the parametric model in (29) was then fit to this data. The tangential component could not be estimated based on these experiments, since no tangential deflection was produced. The results of the ten experiments, as well as the fit model are shown in Figure 7.

In order to assess the quality of the fit, which visually appears accurate, statistics were generated and are shown in Table 1. Relevant statistical quantities used in the paper are defined in Appendix B.1. The model appears to fit the normal loading path data well.

6.3 Linear Loading Path Experiments

Forty-five linear loading path experiments were performed. In each experiment, the pusher compressed the compliant material at a constant ratio between normal and tangential deflection. The material was compressed at fifteen different angles in the (δ_n, δ_t) plane ranging from two degrees to 30 degrees in increments of two. Each angle was repeated three times.

[4]Shore A is a scale for measuring Durometer hardness which is the international standard for measuring the hardness of rubber, plastic, and most nonmetallic materials. For the intuition sake, 40 on Shore A scale corresponds to the hardness of common pencil eraser

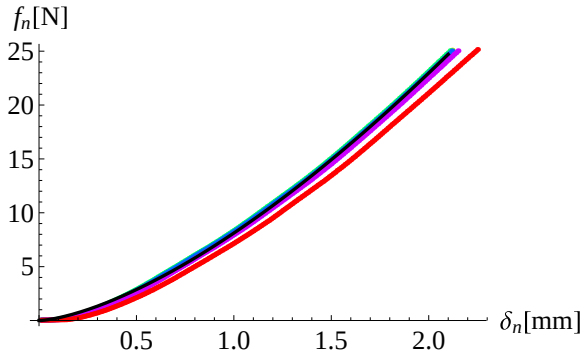

Figure 7: Model fit ($k_n = 8.119$) and data for normal loading path experiments

Table 1: Normal Loading Path Statistics

R^2	Mean Abs. Err.	Mean Norm. Abs. Err.	Max Err.	Min Err.
.9997	.1677[N]	3.421%	.7523[N]	-.8248[N]

See Figure 8 for the loading paths used in the experiments. Each experiment was run until there was a 25[N] force in the normal direction.

The results of the experiments, along with the fit to the data, is shown in Figure 9. In the tangential direction, we have normalized the force by the square root of the ratio of deflections used in each particular experiment, $\sqrt{c} = \sqrt{\frac{\delta_t}{\delta_n}}$. The reason for this is to visualize the data solely as a function of δ_t and not δ_n, recall from (29) that $f_t\sqrt{c} = k_t\delta_t^{3/2}$.

To assess the quality of the fit we again generate several statistics, independently for the

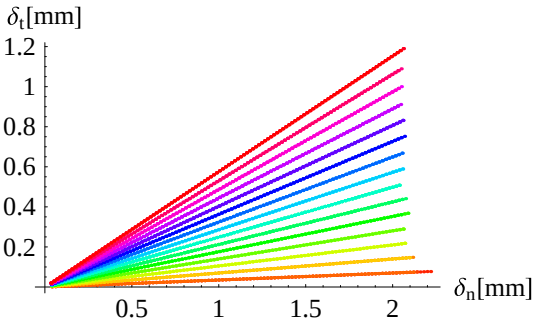

Figure 8: Loading paths for the linear loading experiments

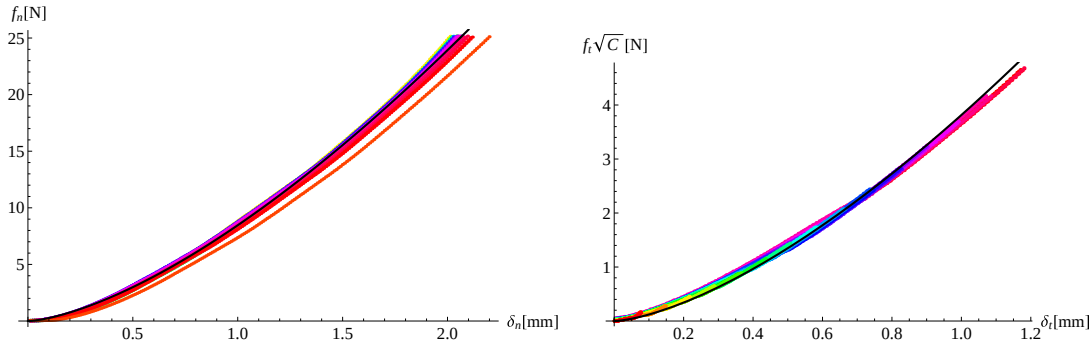

(a) (b)

Figure 9: Component Model fit and data for linear loading path experiments: (a) Normal with $k_n = 8.458$; (b) Tangential with$k_t = 3.814$.

fit in the normal direction and the tangential direction. The statistics are shown in Table 2. Again the fit appears quite good, indicating that our parametric model can adequately predict linear loading path experimental data. This is significant because our experiments violate the small deflection assumption of this model as well as the assumption that two uniformly shaped spheres are in contact. Additionally, the parameter k_n agrees closely with the value fit from the normal loading paths. This is not unexpected, since a normal loading is also a linear loading path.

Table 2: Tangential Loading Path Statistics,normal & tangential fits

	R^2	Mean Abs. Err.	Mean Norm. Abs. Err.	Max Err.	Min Err.
Normal	.9996	.2326[N]	5.21%	1.187[N]	-2.241[N]
Tan.	.9977	.0482[N]	13.02%	.1439[N]	-.2036[N]

6.4 Nonlinear Loading Path Experiments

One hundred and fifty nonlinear loading path experiments were performed, in three sets of fifty, which we denote Set 1,2, and 3. Each nonlinear experiment consisted of two linear segments. In each set of fifty experiments, five points in the (δ_n, δ_t) plane were chosen, equally spaced along linear loading path at 20 degrees, which we term *convergence points*. Five different loading paths converged on each of these five points at different angles, and each loading path was repeated twice, for a total of fifty experiments. See Figure 10 for the loading

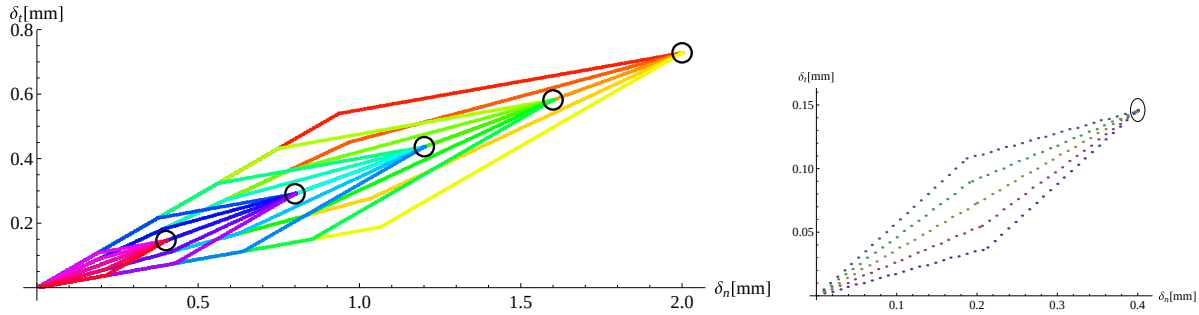

(a) (b)

Figure 10: Loading path experiments for nonlinear loading Set 1: (a) The five convergence points are the five points on the linear loading path where the loading paths converge together; (b) enlargement of the five different pathes to the first convergence point.

Table 3: Nonlinear Loading Path dispersion statistics

	Total Err.	Mean Norm. Err.
Set 1	10.28[N]	1.8 %
Set 2	9.28[N]	3.6 %
Set 3	4.61[N]	1.0 %

paths used in Set 1 experiments. The convergence points in this figure are the common points where the paths intersect. In the nonlinear loading Set 1 experiments, the approach angle ranged from 10 to 30 degrees in increments of five degrees. In the Set 2 experiments, the approach angles ranged from 16 to 24 Degrees in increments of two degrees, and finally in the Set 3 experiments, the approach angle ranged from 18 to 22 degrees in increments of 1 degree. Therefore the nonlinear loading experiments become closer to linear paths as we move from Set 1 to Set 3. The data points from all loading paths at the loading path convergence points are shown in Figure 11 along with fits to the linear loading path data in each experiment set. The data appears linear in the (f_n, f_t) plane due to the equivalent dependence of each force component on its respective displacement. Critically, *no model* which has as its only state δ_n, δ_t can predict the dispersion of the data at the convergence points, since these points are at the same position in the (δ_n, δ_t) plane. Statistics characterizing the dispersion of these points is shown in Table 3. See Appendix B.2 for a description of each statistic.

The dispersion of the data points decreases as the loading paths approach linear loading paths, as would be expected. For the large loading path variations in Set 1, the data is visibly spread apart, however, the mean normalized error, characterizing this spread is only

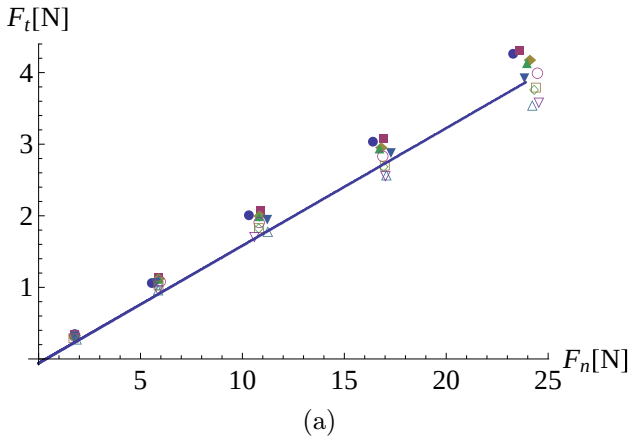

(a)

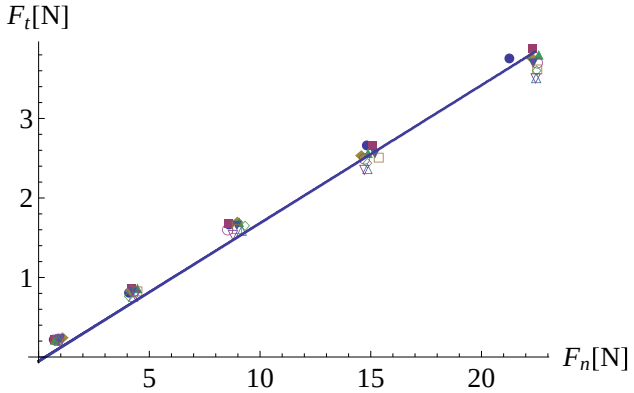

(b)

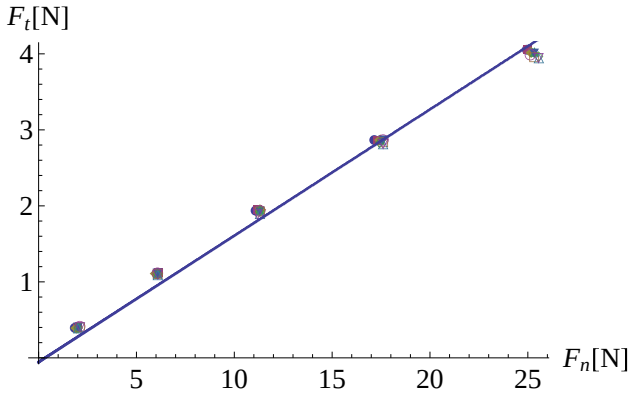

(c)

Figure 11: Nonlinear loading path convergence point data and model fit:
(a) Set 1: 15 Degree Range; (b) Set 2: 10 Degree Range; (c) Set 3: 5 Degree Range.

1.8%. This indicates that if the linear loading path model was used to predict the forces for the nonlinear loading paths at the convergence point, on average this model would only be incorrect by 1.8%. The reason for the unexpected larger mean normalized error of Set 2 is that the zero displacement changed and the experiment begun in smaller displacements and smaller forces. Therefore the means of the forces are also smaller than in the other sets, hence increasing the mean normalized error.

7 Conclusion

The Hertz-Walton contact model allows concise analytic representation of the contact forces as a function of the contact point displacements. Based on the contact model, we derived contact stiffness matrices, which are asymmetric matrices. As a result the grasp stiffness matrix of the entire grasp is asymmetric. We obtained a concise condition for the global asymptotic stability of the grasp linearized dynamics, and therefore a local asymptotic stability for the nonlinear system. The contact model and the grasp stability analysis seem to extend to $3D$ grasps under a hard-finger model (i.e. no frictional torque about the contact normal). Finally, we are in process of constructing an experimental grasp arrangement for testing our theoretical predictions [2].

A Details of Grasp Stability Analysis

This appendix contains proofs of several results stated in Section 4 and Section 5. The first results concerns the linearized grasp dynamics under the Hertz-Walton compliance model. We begin with a preliminary lemma concerning $D^2X_{r_i}$.

Lemma A.1. *Let $X_{r_i}(q) = R(\theta)r_i + d$ be the position of the i^{th} contact such that $q = (d, \theta)$ is $\mathcal{B}$'s configuration and $r_i \in \mathcal{B}$ is held fixed. The action of $D^2X_{r_i}^T(q)$ on f_i is the 3×3 matrix:*

$$D^2X_{r_i}^T(q)f_i = \begin{bmatrix} O & 0 \\ 0^T & -\boldsymbol{\rho}_i \cdot f_i \end{bmatrix},$$

where O is a 2×2 matrix of zeroes.

Proof: It can be verified that the Jacobian of $X_{r_i}(q)$ is the 2×3 matrix $DX_{r_i}(q) = [I\ J\boldsymbol{\rho}_i(\theta)]$, where I is a 2×2 identity matrix, $J = \left[\begin{smallmatrix} 0 & -1 \\ 1 & 0 \end{smallmatrix}\right]$, and $\boldsymbol{\rho}_i(\theta) = R(\theta)r_i$. To obtain a formula for $D^2X_{r_i}(q)$, we compute the derivative of $DX_{r_i}(q)$ along a c-space trajectory $q(t)$. Recall that $\mathcal{B}$'s velocity along $q(t)$ is denoted $\dot{q} = (v, \omega)$, where $v \in I\!R^2$ and $\omega \in I\!R$ are

$\mathcal{B}$'s linear and angular velocities. Then $\frac{d}{dt}DX_{r_i}(q(t)) = \begin{bmatrix} O & J\dot{R}r_i \end{bmatrix} = \begin{bmatrix} O & -\boldsymbol{\rho}_i\omega \end{bmatrix}$, where we used the formula $\dot{R}r_i = \omega JRr_i$ and the identity $J^2 = -I$. The action of this derivative on f_i is: $\left(\frac{d}{dt}DX_{r_i}^T(q(t))\right)f_i = \begin{pmatrix} 0 \\ (-\boldsymbol{\rho}_i \cdot f_i)\omega \end{pmatrix}$. On the other hand, $\frac{d}{dt}DX_{r_i}(q(t)) = (D^2X_{r_i}(q))\dot{q}$ by the chain rule. Hence the action of $D^2X_{r_i}(q)$ on f_i is the 3×3 matrix:

$$D^2X_{r_i}^T(q)f_i = \begin{bmatrix} O & 0 \\ 0^T & -\boldsymbol{\rho}_i \cdot f_i \end{bmatrix},$$

where O is a 2×2 matrix of zeroes. □

The following proposition specifies the linearized grasp dynamics under the Hertz-Walton compliance model.

Proposition 4.1. *Let a quasi-rigid body $\mathcal{B}$ be held at an equilibrium grasp configuration, $q_0 = (d_0, \theta_0)$, by quasi-rigid bodies $\mathcal{A}_1, \ldots, \mathcal{A}_k$. Let $\Delta p_1 = q - q_0$ and $\Delta p_2 = \dot{q} - 0$. The* **linearized dynamics** *of $\mathcal{B}$ at $(q_0, 0)$ is given by*

$$\frac{d}{dt}\begin{pmatrix}\Delta p_1 \\ \Delta p_2\end{pmatrix} = \begin{bmatrix} O_{3\times3} & I_{3\times3} \\ -M^{-1}(q_0)K_p(q_0,0) & -M^{-1}(q_0)K_d(q_0,0)\end{bmatrix}\begin{pmatrix}\Delta p_1 \\ \Delta p_2\end{pmatrix}, \tag{30}$$

where K_p and K_d are the grasp stiffness and damping matrices. The grasp stiffness matrix is the **asymmetric** *3×3 matrix:*

$$K_p(q_0,0) = -\sum_{i=1}^{k}\left\{\tilde{K}_i(q_0) - \begin{bmatrix} O_{2\times2} & 0 \\ 0^T & \boldsymbol{\rho}_i(\theta_0)\cdot f_i \end{bmatrix} + G_i^T(q_0)\begin{bmatrix} f_i^n & f_i^t \\ -f_i^t & f_i^n \end{bmatrix} Dn_i(q_0)\right\}, \tag{31}$$

where $\tilde{K}_i(q_0)$ is the i^{th} contact c-space stiffness matrix, $\boldsymbol{\rho}_i(\theta_0)$ is the i^{th} contact position relative to $\mathcal{B}$'s origin, f_i is the i^{th} contact force with components (f_i^t, f_i^n), and n_i is the i^{th} contact normal $(i = 1 \ldots k)$. The grasp damping matrix is the symmetric 3×3 matrix:

$$K_d(q_0,0) = \sum_{i=1}^{k}\delta_i^n(q_0)G_i^T(q_0)R_i(q_0)\begin{bmatrix} \frac{\partial\varphi_i^t}{\partial\dot{\delta}_i^t}(0) & 0 \\ 0 & \frac{\partial\varphi_i^n}{\partial\dot{\delta}_i^n}(0)\end{bmatrix}R_i^T(q_0)G_i(q_0), \tag{32}$$

where φ_i^t and φ_i^n are the tangential and normal damping functions at the i^{th} contact $(i = 1 \ldots k)$.

Proof: First consider the linearization of $M^{-1}(p_1)$ and $C(p_1, p_2)$ in (10). The net wrench acting on $\mathcal{B}$, $\sum_{i=1}^{k} G_i^T f_i$, vanishes at $p_1 = q_0$. Moreover, $C(p_1, p_2)$ is quadratic and homogenous

in p_2, therefore it vanishes at $p_2=0$. It follows from these two facts that the linearization of $M^{-1}(p_1)$ and $C(p_1,p_2)$ vanish at $(q_0,0)$. Thus we only need to compute the matrices:

$$K_p(q_0,0) = -\frac{\partial}{\partial p_1}\Big|_{\substack{p_1=q_0\\p_2=0}} \sum_{i=1}^k G_i^T(p_1) f_i(p_1,p_2)$$
$$K_d(q_0,0) = -\frac{\partial}{\partial p_2}\Big|_{\substack{p_1=q_0\\p_2=0}} \sum_{i=1}^k G_i^T(p_1) f_i(p_1,p_2),$$

where the minus signs will allow us to write the linearized dynamics in the standard form (15). First consider the matrix $K_p(q_0,0)$. Since $G_i(p_1)=DX_{r_i}(p_1)$, the derivative $\frac{\partial}{\partial p_1} G_i^T(p_1) f_i(p_1,p_2)$ is given by

$$\frac{\partial}{\partial p_1} G_i^T(p_1) f_i(p_1,p_2) = D^2 X_{r_i}^T(p_1) f_i(p_1,p_2) + G_i^T \frac{\partial}{\partial p_1} f_i(p_1,p_2).$$

A formula for $D^2X_{r_i}^T(p_1)f_i(p_1,p_2)$ is specified in Lemma A.1. Next consider the term $G_i^T \frac{\partial}{\partial p_1} f_i(p_1,p_2)$. Using the notation $\boldsymbol{\delta}_i = (\delta_i^t, \delta_i^n)$ and $\dot{\boldsymbol{\delta}}_i = (\dot\delta_i^t, \dot\delta_i^n)$, the i^{th} contact force is given by

$$f_i(p_1,p_2) = R_i(p_1) \begin{pmatrix} f_i^t\big(\boldsymbol{\delta}_i(p_1), \dot{\boldsymbol{\delta}}_i(p_1,p_2)\big) \\ f_i^n\big(\boldsymbol{\delta}_i(p_1), \dot{\boldsymbol{\delta}}_i(p_1,p_2)\big) \end{pmatrix} \quad \text{where } R_i(p_1) = [t_i\, n_i].$$

Hence $\frac{\partial}{\partial p_1} f_i(p_1,p_2)$ is given by

$$\begin{aligned} \tfrac{\partial}{\partial p_1} f_i(p_1,p_2) &= \big(DR_i(p_1)\big) \begin{pmatrix} f_i^t(\boldsymbol{\delta}_i, \dot{\boldsymbol{\delta}}_i) \\ f_i^n(\boldsymbol{\delta}_i, \dot{\boldsymbol{\delta}}_i) \end{pmatrix} \\ &+ R_i(p_1) \left\{ \begin{pmatrix} \frac{\partial}{\partial \boldsymbol{\delta}_i} f_i^t(\boldsymbol{\delta}_i, \dot{\boldsymbol{\delta}}_i) \\ \frac{\partial}{\partial \boldsymbol{\delta}_i} f_i^n(\boldsymbol{\delta}_i, \dot{\boldsymbol{\delta}}_i) \end{pmatrix} D\boldsymbol{\delta}_i(p_1) + \begin{pmatrix} \frac{\partial}{\partial \dot{\boldsymbol{\delta}}_i} f_i^t(\boldsymbol{\delta}_i, \dot{\boldsymbol{\delta}}_i) \\ \frac{\partial}{\partial \dot{\boldsymbol{\delta}}_i} f_i^n(\boldsymbol{\delta}_i, \dot{\boldsymbol{\delta}}_i) \end{pmatrix} \tfrac{\partial}{\partial p_1} \dot{\boldsymbol{\delta}}_i(p_1,p_2) \right\}. \end{aligned} \tag{33}$$

Consider the first summand in (33). Since $t_i = J^T n_i$, the matrix $R_i = [t_i\, n_i]$ can be written as $R_i = [J^T n_i\, n_i]$, where $J = \left[\begin{smallmatrix} 0 & -1 \\ 1 & 0 \end{smallmatrix}\right]$. Thus $DR(q_0) = [J^T Dn_i(q_0)\, Dn_i(q_0)]$, and consequently $\big(DR_i(q_0)\big)\left(\begin{smallmatrix} f_i^t \\ f_i^n \end{smallmatrix}\right) = (f_i^t J^T + f_i^n I) Dn_i(q_0)$, where I is a 2×2 identity matrix. Next consider the second summand in (33). According to the Hertz-Walton model, the force components (f_i^t, f_i^n) are given by

$$\begin{pmatrix} f_i^t(\boldsymbol{\delta}_i, \dot{\boldsymbol{\delta}}_i) \\ f_i^n(\boldsymbol{\delta}_i, \dot{\boldsymbol{\delta}}_i) \end{pmatrix} = \begin{pmatrix} -h_i(\delta_i^t, \delta_i^n) \\ g_i(\delta_i^n) \end{pmatrix} + \begin{pmatrix} -\delta_i^n \cdot \varphi_i^t(\dot\delta_i^t) \\ \delta_i^n \cdot \varphi_i^n(\dot\delta_i^n) \end{pmatrix}. \tag{34}$$

The derivative of (f_i^t, f_i^n) with respect to $\boldsymbol{\delta}_i$ at $(q_0,0)$ is given by

$$\begin{pmatrix} \frac{\partial}{\partial \boldsymbol{\delta}_i} f_i^t(\boldsymbol{\delta}_i, \dot{\boldsymbol{\delta}}_i) \\ \frac{\partial}{\partial \boldsymbol{\delta}_i} f_i^n(\boldsymbol{\delta}_i, \dot{\boldsymbol{\delta}}_i) \end{pmatrix}\Big|_{\substack{p_1=q_0\\p_2=0}} = K_i(q_0) + \begin{bmatrix} 0 & -\varphi_i^t(\dot\delta_i^t) \\ 0 & \varphi_i^n(\dot\delta_i^n) \end{bmatrix}\Big|_{\substack{p_1=q_0\\p_2=0}} = K_i(q_0),$$

where we used the fact that $\dot{\delta}_i^t = \dot{\delta}_i^n = 0$ at $p_2 = 0$, and consequently $\varphi_i^t(0) = \varphi_i^n(0) = 0$. The Jacobian $D\boldsymbol{\delta}_i(p_1)$ appearing in the second summand of (33) is given by $D\boldsymbol{\delta}_i = \left[\begin{smallmatrix} t_i^T \\ -n_i^T \end{smallmatrix}\right] G_i$ (see proof of Lemma 3.1). As for the third summand in (33), $\dot{\boldsymbol{\delta}}_i = \left[\begin{smallmatrix} t_i^T \\ -n_i^T \end{smallmatrix}\right] G_i p_2$, and consequently $\frac{\partial}{\partial p_1}\dot{\boldsymbol{\delta}}_i(p_1, p_2) = 0$ at $p_2 = 0$. Substituting these terms in (33), then summing the expressions $D^2 X_{r_i}^T(p_1) f_i(p_1, p_2) + G_i^T \frac{\partial}{\partial p_1} f_i(p_1, p_2)$ over $i = 1 \dots k$ gives

$$\begin{aligned} K_p(q_0, 0) &= -\frac{\partial}{\partial p_1}\Big|_{\substack{p_1 = q_0 \\ p_2 = 0}} \sum_{i=1}^k G_i^T(p_1) f_i(p_1, p_2) \\ &= -\sum_{i=1}^k \Big\{ G_i^T(q_0) R_i(q_0) K_i(q_0) \left[\begin{smallmatrix} t_i^T \\ -n_i^T \end{smallmatrix}\right] G_i(q_0) \\ &\quad - \begin{bmatrix} O & 0 \\ 0^T & \boldsymbol{\rho}_i(\theta_0) \cdot f_i \end{bmatrix} + G_i^T(q_0)(f_i^t J^T + f_i^n I) D n_i(q_0) \Big\}, \end{aligned}$$

where we substituted $D^2 X_{r_i}^T(q_0) f_i = \left[\begin{smallmatrix} O & 0 \\ 0^T & -\boldsymbol{\rho}_i \cdot f_i \end{smallmatrix}\right]$ in accordance with Lemma A.1. Based on the proof of Lemma 3.1, $\tilde{K}_i = G_i^T(q_0) R_i(q_0) K_i(q_0) \left[\begin{smallmatrix} t_i^T \\ -n_i^T \end{smallmatrix}\right] G_i(q_0)$. Substituting for this term gives the formula

$$K_p(q_0, 0) = -\sum_{i=1}^k \left\{ \tilde{K}_i(q_0) - \begin{bmatrix} O & 0 \\ 0^T & \boldsymbol{\rho}_i(\theta_0) \cdot f_i \end{bmatrix} + G_i^T(q_0)(f_i^t J^T + f_i^n I) D n_i(q_0) \right\}.$$

Finally consider the matrix $K_d(q_0, 0)$. We have to compute the derivative:

$$\frac{\partial}{\partial p_2}\Big|_{\substack{p_1 = q_0 \\ p_2 = 0}} G_i^T(p_1) f_i(p_1, p_2) = G_i^T(p_1) \frac{\partial}{\partial p_2}\Big|_{\substack{p_1 = q_0 \\ p_2 = 0}} f_i(p_1, p_2).$$

Based on (34),

$$\frac{\partial}{\partial p_2} f_i(p_1, p_2) = R_i(p_1) \begin{bmatrix} -\delta_i^n(p_1) \cdot \frac{\partial}{\partial \dot{\delta}_i^t} \varphi_i^t(\dot{\delta}_i^t) & 0 \\ 0 & \delta_i^n(p_1) \cdot \frac{\partial}{\partial \dot{\delta}_i^n} \varphi_i^n(\dot{\delta}_i^n) \end{bmatrix} \frac{\partial}{\partial p_2} \dot{\boldsymbol{\delta}}_i(p_1, p_2).$$

Since $\dot{\boldsymbol{\delta}}_i = \left[\begin{smallmatrix} t_i^T \\ -n_i^T \end{smallmatrix}\right] G_i p_2$, we have that $\frac{\partial}{\partial p_2}\dot{\boldsymbol{\delta}}_i(p_1, p_2) = \left[\begin{smallmatrix} t_i^T \\ -n_i^T \end{smallmatrix}\right] G_i$. Hence

$$\begin{aligned} \frac{\partial}{\partial p_2}\Big|_{\substack{p_1 = q_0 \\ p_2 = 0}} f_i(p_1, p_2) &= \delta_i^n(q_0) R_i(q_0) \begin{bmatrix} -\frac{\partial \varphi_i^t}{\partial \dot{\delta}_i^t}(0) & 0 \\ 0 & \frac{\partial \varphi_i^n}{\partial \dot{\delta}_i^n}(0) \end{bmatrix} \left[\begin{smallmatrix} t_i^T \\ -n_i^T \end{smallmatrix}\right] G_i(q_0) \\ &= -\delta_i^n(q_0) R_i(q_0) \begin{bmatrix} \frac{\partial \varphi_i^t}{\partial \dot{\delta}_i^t}(0) & 0 \\ 0 & \frac{\partial \varphi_i^n}{\partial \dot{\delta}_i^n}(0) \end{bmatrix} R_i^T(q_0) G_i(q_0), \end{aligned}$$

where we substituted $R_i^T = \left[\begin{smallmatrix} t_i^T \\ n_i^T \end{smallmatrix}\right]$. Summing over the k contacts,

$$\begin{aligned} K_d(q_0,0) &= -\tfrac{\partial}{\partial p_2}\Big|_{\substack{p_1=q_0 \\ p_2=0}} \sum_{i=1}^k G_i^T(p_1) f_i(p_1,p_2) \\ &= \sum_{i=1}^k \delta_i^n(q_0) G_i^T(q_0) R_i(q_0) \begin{bmatrix} \frac{\partial \varphi_i^t}{\partial \tilde{\delta}_i^t}(0) & 0 \\ 0 & \frac{\partial \varphi_i^n}{\partial \tilde{\delta}_i^n}(0) \end{bmatrix} R_i^T(q_0) G_i(q_0). \end{aligned}$$

□

The following lemma specifies the grasp stiffness matrix in the case where $\mathcal{B}$ is held along planar facets.

Lemma 5.1. *When $\mathcal{B}$ is held in equilibrium grasp along planar facets, the grasp stiffness matrix specified in eq. (31) becomes*

$$K_p(q_0,0) = -\sum_{i=1}^k \tilde{K}_i(q_0), \tag{35}$$

where $\tilde{K}_i(q_0)$ is the i^{th} c-space contact stiffness matrix for $i = 1 \ldots k$.

Proof: The stiffness matrix K_p is specified in (31) as

$$K_p(q_0,0) = -\sum_{i=1}^k \left\{ \tilde{K}_i(q_0) - \begin{bmatrix} O_{2\times 2} & 0 \\ 0^T & \boldsymbol{\rho}_i \cdot f_i \end{bmatrix} + G_i^T(q_0) \begin{bmatrix} f_i^n & f_i^t \\ -f_i^t & f_i^n \end{bmatrix} Dn_i(q_0) \right\}. \tag{36}$$

Consider the third summand in (36). The 2×3 Jacobian $Dn_i(q_0)$ is specified in eq. (14) as

$$Dn_i(q_0) = \frac{1}{r_{\mathcal{A}_i} + r_{\mathcal{B}_i} - \delta_i^n(q_0)} \left[I - n_i n_i^T,\ (r_{\mathcal{B}_i} + \boldsymbol{\rho}_i(\theta_0) \cdot n_i) J n_i \right],$$

where $J = \left[\begin{smallmatrix} 0 & -1 \\ 1 & 0 \end{smallmatrix}\right]$. Substituting $r_{\mathcal{B}_i} = \infty$ for the flat facets of $\mathcal{B}$ gives $Dn_i(q_0) = [O\ J n_i]$. The third summand in K_p thus becomes

$$\begin{aligned} &\textstyle\sum_{i=1}^k G_i^T(q_0) \begin{bmatrix} f_i^n & f_i^t \\ -f_i^t & f_i^n \end{bmatrix} Dn_i(q_0) \\ &= \textstyle\sum_{i=1}^k G_i^T(q_0) \left(f_i^t J^T + f_i^n I \right) [O\ J n_i] = \left[O_{3\times 2},\ \sum_{i=1}^k G_i^T(q_0)(f_i^t n_i + f_i^n J n_i) \right] \\ &= \left[O_{3\times 2},\ \textstyle\sum_{i=1}^k G_i^T(q_0) J (f_i^t t_i + f_i^n n_i) \right] = \left[O_{3\times 2},\ \sum_{i=1}^k G_i^T(q_0) J f_i \right], \end{aligned}$$

where we used the relations $t_i = J^T n_i$ and $f_i = f_i^t t_i + f_i^n n_i$. The 2×3 Jacobian $G_i = DX_{r_i}(q_0)$ is given by $G_i = [I\ J\boldsymbol{\rho}_i]$. Substituting for G_i gives

$$\sum_{i=1}^{k} G_i^T(q_0) J f_i = \sum_{i=1}^{k} \begin{bmatrix} I \\ \boldsymbol{\rho}_i^T J^T \end{bmatrix} J f_i = \begin{bmatrix} J\sum_{i=1}^{k} f_i \\ \sum_{i=1}^{k} \boldsymbol{\rho}_i^T J^T J f_i \end{bmatrix} = \begin{bmatrix} \vec{0} \\ \sum_{i=1}^{k} \boldsymbol{\rho}_i \cdot f_i \end{bmatrix},$$

since $\sum_{i=1}^{k} f_i = \vec{0}$ at the equilibrium grasp. The curvature dependent term in K_p is thus

$$\sum_{i=1}^{k} G_i^T(q_0) \begin{bmatrix} f_i^n & f_i^t \\ -f_i^t & f_i^n \end{bmatrix} Dn_i(q_0) = \begin{bmatrix} O_{2\times 2} & 0 \\ 0^T & \sum_{i=1}^{k} \boldsymbol{\rho}_i \cdot f_i \end{bmatrix}.$$

When this term is substituted into (36), one obtains that $K_p(q_0, 0) = -\sum_{i=1}^{k} \tilde{K}_i(q_0)$. □

The following proposition specifies the relation between the symmetric and asymmetric parts of the matrix A which guarantees the stability condition $\gamma < \sqrt{\alpha}\beta$.

Proposition 5.2. *Let $\mathcal{B}$ be held along planar facets in a k-finger grasp, such that $\delta_i^n(q_0) \cong \delta_c^n$ and $c_i \cong c$ for $i = 1 \ldots k$. Let $\alpha > 0$ and $\beta > 0$ for the given grasp. The condition $\gamma < \sqrt{\alpha}\beta$ is satisfied when A_s and A_{as} satisfy the condition:*

$$\|A_{as}\| < \kappa_d \frac{\lambda_{min}(\bar{M})}{\lambda_{max}(\bar{M})} \sqrt{\lambda_{min}(A_s)},$$

where A is specified in (25), κ_d is the damping parameter, and $\bar{M}$ is $\mathcal{B}$'s scaled inertia matrix.

Proof: Consider the condition $\gamma < \sqrt{\alpha}\beta$ specified in eq. (22). The term α on the right side of this condition can be written as

$$\alpha = \lambda_{min}(\bar{M}^{-\frac{1}{2}}(\bar{K}_p)_s \bar{M}^{-\frac{1}{2}}) = \min_{\|v\|=1} \left\{ v^T \bar{M}^{-\frac{1}{2}}(\bar{K}_p)_s \bar{M}^{-\frac{1}{2}} v \right\}.$$

Substituting for $(\bar{K}_p)_s$ according to (23) gives

$$\lambda_{min}\big(\bar{M}^{-1/2}(\bar{K}_p)_s \bar{M}^{-1/2}\big) \geq \sqrt{\delta_c^n}\lambda_{min}\big(A_s\big) \cdot \min_{\|v\|=1} \left\{ v^T \bar{M}^{-\frac{1}{2}} \big(\sum_{i=1}^{k} S^T G_i^T G_i S \big) \bar{M}^{-\frac{1}{2}} v \right\}, \quad (37)$$

where we substituted $R_i R_i^T = I$ for $i = 1 \ldots k$. Without loss of generality, let the world and $\mathcal{B}$'s frames be located at the grasp's centroid. Under this assumption the position of the finger contacts in $\mathcal{B}$'s frame is identical to their position in the world frame, $x_i = \boldsymbol{\rho}_i(\theta_0)$ for

$i=1\ldots k$, while $x_c=\vec{0}$. The Jacobian G_i is given by the 2×3 matrix $G_i=DX_{r_i}=[I\ Jx_i]$, where I is a 2×2 identity matrix and $J=\left[\begin{smallmatrix} 0 & -1 \\ 1 & 0 \end{smallmatrix}\right]$. Hence

$$\begin{aligned}\textstyle\sum_{i=1}^k S^T G_i^T G_i S &= \textstyle\sum_{i=1}^k \begin{bmatrix} I & 0 \\ 0^T & 1/l_c \end{bmatrix} \begin{bmatrix} I \\ x_i^T J^T \end{bmatrix} [I\ Jx_i] \begin{bmatrix} I & 0 \\ 0^T & 1/l_c \end{bmatrix} \\ &= \begin{bmatrix} kI & \frac{1}{l_c} J \sum_{i=1}^k x_i \\ \frac{1}{l_c}(\sum_{i=1}^k x_i)^T J^T & \frac{1}{l_c^2}\sum_{i=1}^k \|x_i\|^2 \end{bmatrix} \\ &= k \begin{bmatrix} I & \frac{1}{l_c} Jx_c \\ \frac{1}{l_c} x_c^T J^T & \frac{1}{kl_c^2}\sum_{i=1}^k \|x_i\|^2 \end{bmatrix} = kI_{3\times 3},\end{aligned}$$

where we substituted $x_c=\frac{1}{k}\sum_{i=1}^k x_i=\vec{0}$ and $l_c^2=\frac{1}{k}\sum_{i=1}^k \|x_i\|^2$. The matrix $\sum_{i=1}^k S^T G_i^T G_i S$ is thus essentially the identity matrix. Substituting this matrix is into (37) gives

$$\lambda_{min}\big(\bar{M}^{-1/2}(\bar{K}_p)_s\bar{M}^{-1/2}\big) \geq k\sqrt{\delta_c^n}\lambda_{min}(A_s)\lambda_{min}(\bar{M}^{-1}), \tag{38}$$

where $\lambda_{min}(\bar{M}^{-1})=\min_{\|v\|=1}\{v^T\bar{M}^{-1}v\}$. Next consider the quantity γ on the left side (22),

$$\begin{aligned}\gamma^2=\|\bar{M}^{-\frac{1}{2}}(\bar{K}_p)_{as}\bar{M}^{-\frac{1}{2}}\|^2 &= \lambda_{max}\left((\bar{M}^{-\frac{1}{2}}(\bar{K}_p)_{as}\bar{M}^{-\frac{1}{2}})^T\bar{M}^{-\frac{1}{2}}(\bar{K}_p)_{as}\bar{M}^{-\frac{1}{2}}\right) \\ &= \lambda_{max}\left(\bar{M}^{-\frac{1}{2}}(\bar{K}_p)_{as}^T\bar{M}^{-1}(\bar{K}_p)_{as}\bar{M}^{-\frac{1}{2}}\right).\end{aligned}$$

In general, when P and Q are symmetric matrices, $\lambda_{max}(P^TQP)\leq\lambda_{max}(Q)\lambda_{max}(P^TP)$. Applying this inequality twice gives

$$\begin{aligned}\|\bar{M}^{-\frac{1}{2}}(\bar{K}_p)_{as}\bar{M}^{-\frac{1}{2}}\|^2 &\leq \lambda_{max}(\bar{M}^{-1})\cdot\lambda_{max}\left(\bar{M}^{-\frac{1}{2}}(\bar{K}_p)_{as}^T(\bar{K}_p)_{as}\bar{M}^{-\frac{1}{2}}\right) \\ &\leq \lambda_{max}^2(\bar{M}^{-1})\cdot\lambda_{max}\left((\bar{K}_p)_{as}^T(\bar{K}_p)_{as}\right).\end{aligned}$$

Substituting for $(\bar{K}_p)_{as}$ according to (24) gives

$$\begin{aligned}&\|\bar{M}^{-\frac{1}{2}}(\bar{K}_p)_{as}\bar{M}^{-\frac{1}{2}}\|^2 \leq \\ &\delta_c^n\lambda_{max}^2(\bar{M}^{-1})\|A_{as}\|^2\cdot\max_{\|v\|=1}\left\{v^T\big(\textstyle\sum_{i=1}^k S^TG_i^TG_iS\big)^T\big(\sum_{i=1}^k S^TG_i^TG_iS\big)v\right\}.\end{aligned}$$

Since $\sum_{i=1}^k S^TG_i^TG_iS=kI$, we obtain that

$$\gamma=\|\bar{M}^{-1/2}(\bar{K}_p)_{as}\bar{M}^{-1/2}\|\leq k\sqrt{\delta_c^n}\lambda_{max}(\bar{M}^{-1})\|A_{as}\|.$$

When the bound on γ is combined with the bound on α specified in (38), the condition $\gamma<\sqrt{\alpha}\beta$ is implied by the inequality:

$$\|A_{as}\|<\kappa_d\frac{\lambda_{min}(\bar{M})}{\lambda_{max}(\bar{M})}\sqrt{\lambda_{min}(A_s)},$$

where we canceled the common factor $k\sqrt{\delta_c^n}$ from both sides of the inequality and substituted $\lambda_{min}(\bar{M}^{-1}) = 1/\lambda_{max}(\bar{M})$ and $\lambda_{max}(\bar{M}^{-1}) = 1/\lambda_{min}(\bar{M})$. □

B Statistical quantities

B.1 Normal and linear loading path statistics

1. R^2- coefficient of determination as reported by Mathematica ©.
2. Mean Abs. Err. - $\frac{1}{n}\sum_{i=1}^{n} \|f_{d_i} - f_{m_i}(\delta_t, \delta_n)\|$
   where f_{d_i} is the i^{th} force data point, of either normal force or tangential force, f_{m_i} is the model's prediction of force, and n is the number of data points.
3. Mean Norm. Abs. Err. - $\frac{1}{n}\sum_{i=1}^{n} \|\frac{f_{d_i} - f_{m_i}(\delta_t, \delta_n)}{f_{m_i}}\|$.
4. Max Err. - $\max_i(f_{d_i} - f_{m_i})$.
5. Min Err. - $\min_i(f_{d_i} - f_{m_i})$.

B.2 Nonlinear loading path statistics

1. Total Err. - $\sum_i \sum_j \|(f_{n_{ij}}, f_{t_{ij}}) - (\mu_{n_j}, \mu_{t_j})\|_2$
   where $(f_{n_{ij}}, f_{t_{ij}})$ is the i^{th} force data point at the j^{th} convergence point with normal and tangential component respectively and (μ_{n_j}, μ_{t_j}) is the mean force at the j^{th} convergence point.
2. Mean Norm. Err. - $\frac{1}{n}\sum_i \sum_j \frac{\|(f_{n_{ij}}, f_{t_{ij}}) - (\mu_{n_j}, \mu_{t_j})\|_2}{\|(\mu_{n_j}, \mu_{t_j})\|_2}$

References

[1] A. Bicchi. Hands for dexterous manipulation and robust grasping: A difficult road toward simplicity. *IEEE Trans. on Robotics and Automation*, 16(6):652–662, 2000.

[2] J. W. Burdick, Y. Liang, and E. Rimon. Experiments in fixturing mechanics. In *IEEE Int. Conf. on Robotics and Automation*, pages 2579–2585, 2003.

[3] P. Campbell. *Basic Fixture Design.* Industrial Press, New York, 1994.

[4] Y.-C. Chou, V. Chandru, and M. M. Barash. A mathematical approach to automatic configuration of machining fixtures: Analysis and synthesis. *ASME J. of Engineering for Industry*, 111:299–306, 1989.

[5] M. R. Cutkosky and I. Kao. Computing and controlling the compliance of a robotic hand. *IEEE Trans. on Robotics and Automation*, 5(2):151–165, 1989.

[6] D. Elata and J. G. Berryman. Contact force-displacement laws and the mechanical behavior of random packs of identical spheres. *Mechanics of Materials*, 24:229–240, 1996.

[7] B. Fang, R. E. DeVor, and S. G. Kapoor. An elastodynamic model of frictional contact and its influence on the dynamics of a worpiece-fixture system. *ASME J. of Manufacturing Science and Engineering*, 123:481–489, 2001.

[8] Y. Funahashi, T. Yamada, M. Tate, and Y. Suzuki. Grasp stability analysis considering the curvatures at contact points. In *IEEE Int. Conf. on Robotics and Automation*, pages 3040–3046, 1996.

[9] J. Halling. *Principals of Tribology.* Macmillan, London, 1975.

[10] K. Harada and M. Kaneko. A sufficient condition for manipulation of enveloping family. *IEEE Trans. on Robotics and Automation*, 18(4):597–607, 2002.

[11] P. Hartman. *Ordinary Differential Equations.* Birkaauser, Boston, MA., 1982.

[12] H. Hertz. On the contact of elastic solids. In *Miscellaneous Papers by H. Hertz (1882).* Macmillan, London, 1896.

[13] M. W. Hirsch and S. Smale. *Differential Equations, Dynamical Systems, and Linear Algebra.* Academic Press, Inc., Orlando, Fla., 1974.

[14] Muammer Koc Ho Choi. Design and feasibility tests of a flexible gripper based on inflatable rubber pockets. *International Journal of Machine Tools & Manufacture*, 46:1350–1361, 2006.

[15] M. J. Hockenberger and E. C. De Meter. Effect of machining fixture design parameters on workpiece displacement. *Manufacturing Review*, 8(1):22–32, 1995.

[16] E. G. Hoffman. *Jig and Fixture Design.* Delmar Publishers, Albany, NY, 1991.

[17] W. S. Howard and V. Kumar. On the stability of grasped objects. *IEEE Trans. on Robotics and Automation*, 12(6):904–917, 1996.

[18] T. Inoue and S. Hirai. Elastic model of deformable fingertip for soft-fingered manipulation. *IEEE Trans. on Robotics*, 22(6):1273–1279, 2006.

[19] K. L. Johnson. *Contact Mechanics*. Cambridge University Press, 1985.

[20] B. Li and S. N. Melkote. An elastic contact model for the prediction of workpiece-fixture contact forces in clamping. *ASME J. of Manufacturing Science and Engineering*, 121:485–493, 1999.

[21] Q. Lin, J. W. Burdick, and E. Rimon. Computation and analysis of natural compliance in grasping and fixturing arrangements. *IEEE Trans. on Robotics and Automation*, 20(4):651–667, 2004.

[22] Q. Lin, J. W. Burdick, and E. Rimon. Constructing minimum deflection fixture arrangements using frame invariant norms. *IEEE Trans. on Automation Science and Engineering*, 3(3):272–286, 2006.

[23] R. D. Mindlin. Compliance of elastic bodies in contact. *Trans. of the ASME*, 71:A–259, 1949.

[24] R. D. Mindlin and H. Deresiewicz. Elastic spheres in contact under varying oblique forces. *ASME J. of Applied Mechanics*, 20:327–344, 1953.

[25] D. J. Montana. The kinematics of contact with compliance. In *IEEE Int. Conf. on Robotics and Automation*, pages 770–774, 1988.

[26] D. J. Montana. Contact stability for two-fingered grasps. *IEEE Trans. on Robotics and Automation*, 8(4):421–230, 1992.

[27] V.-D. Nguyen. Constructing force-closure grasps. *The Int. J. of Robotics Research*, 7(3):3–16, 1988.

[28] T. Omata and K. Nagata. Rigid body analysis of the indeterminate grasp force in power grasps. *IEEE Trans. on Robotics and Automation*, 16(1):46–54, 2000.

[29] A. Pettersson, S. Davis, J.O. Gray, T.J. Dodd, and T. Ohlsson. Design of a magnetorheological robot gripper for handling of delicate food products with varying shapes. *Journal of Food Engineering*, 98:332–338, 2010.

[30] D.G. Caldwell P.Y. Chua, T. Ilschner. Robotic manipulation of food products - a review. *Industrial Robot: An International Journal*, 30:345–354, 2003.

[31] E. Rimon, J. W. Burdick, and T. Omata. A polyhedral bound on the indeterminate contact forces in fixturing and grasping arrangements. *IEEE Trans. on Robotics and Automation*, 22(2):240–255, 2006.

[32] E. Rimon, S. Shoval, and A. Shapiro. Design of a spider robot for motion with quasistatic force constraints. *Autonomous Robots*, 10:279–296, 2001.

[33] A. Shapiro. Stability of second-order asymmetric linear systems with application to robot grasping. *ASME Journal of Applied Mechanics*, 72(6):966–968, November 2005.

[34] A. Shapiro, A. Greenfield, and H. Choset. Frictional compliance model development and experiments for snake robot climbing. In *IEEE Int. Conf. on Robotics and Automation*, pages x–y, 2007.

[35] P. R. Sinha and J. M. Abel. A contact stress model for multifinger grasps of rough objects. *IEEE Trans. on Robotics and Automation*, 8(1):7–22, Feb. 1992.

[36] J. Tian and Y.-B. Jia. Modeling deformable shell-like objects grasped by a robot hand. In *IEEE Int. Conf. on Robotics and Automation*, pages 1297–1302, 2009.

[37] C. D. Tsai and I. Kao. The latency model for viscoelastic contact interface in robotics: Theory and experiments. In *IEEE Int. Conf. on Robotics and Automation*, pages 1291–1296, 2009.

[38] C. D. Tsai, I. Kao, N. Sakamoto, M. Higashimori, and M. Kaneko. Applying viscoelastic contact modeling to grasping task: an experimental case study. In *IEEE/RSJ Int. Conf. on Intelligent Robots and Systems (IROS)*, pages 3737–3743, 2008.

[39] C. D. Tsai, I. Kao, A. Shibata, K. Yoshimoto, M. Higashimori, and M. Kaneko. Experimental study of creep response of viscoelastic contact interface under force control. In *IEEE/RSJ Int. Conf. on Intelligent Robots and Systems (IROS)*, pages 4275–4280, 2010.

[40] E.J. van Henten, J. Hemming, B.A.J. van Tuijl, J.G. Kornet, J. MMeuleman, J. Bontsema, and E.A. van Os. An autonomous robot for harvesting cucumbers in greenhouses. *Autonomous Robots*, 13:241–258, 2002.

[41] K. Walton. The effective elastic moduli of a random packing of spheres. *J. of Mech. Phys. and Solids*, 35(2):213–226, 1987.

[42] Y.-T. Wang and V. Kumar. Simulation of mechanical systems with multiple frictional contacts. *ASME J. Mechanical Design*, 116:571–579, 1994.

[43] C. H. Xiong, Y. F. Li, H. Ding, and Y.-L. Xiong. On the dynamic stability of grasping. *The Int. J. of Robotics Research*, 18(9):951–958, 1999.

[44] C.-H. Xiong, M. Y. Wang, Y. Tang, and Y.-L. Xiong. Compliant grasping with passive forces. *J. of Robotics Systems*, 22(5):271–285, 2005.

[45] N. Xydas, M. Bhagavat, and I. Kao. Study of soft-finger contact mechanics using finite elements analysis and experiments. In *IEEE Int. Conf. on Robotics and Automation*, 2000.

[46] N. Xydas and I. Kao. Modeling of contact mechanics and friction-limit-surfaces for soft fingers in robotics, with experimental results. *The Int. J. of Robotics Research*, 18(8):941–950, 1999.